SOUTHWEST RESEARCH INSTITUTE®

6220 CULEBRA ROAD 78238-5166 • P.O. DRAWER 28510 78228-0510 • SAN ANTONIO, TEXAS, USA • (210) 684-5111 • WWW.SWRI.ORG

Mechanical Engineering Division
January 26, 2018

Professor KT Ramesh
JHU/HEMI Project Director
Johns Hopkins University
3400 N. Charles Street, Malone Hall 149
Baltimore, MD 21218

Reference: SwRI Project No. 18.22787
PO: 2003301962-Mod 1 (Johns Hopkins University)
Cooperative Agreement No. W911NF-12-2-0022 (Army Research Office)

Subject: Delivery of the final report entitled "*The Effect of Interface Treatment on Ceramic Performance and Modeling Dyneema® Subjected to Ballistic Impact (Distribution A Version)*"

Dear Professor Ramesh:

This letter is to inform you that we have completed the work, and the contractual requirements, for Purchase Order 2003301962-Modification 1 to Johns Hopkins University under prime contract W911NF-12-2-0022 to the Army Research Office. Please find enclosed the technical report entitled "*The Effect of Interface Treatment on Ceramic Performance and Modeling Dyneema® Subjected to Ballistic Impact (Distribution A Version),*" documenting the work performed under this effort as required under the statement of work.

I have appreciated the opportunity to work with you on this contract and hope we can continue this work in the future. If you have any questions regarding the final report please contact me at 612-460-4489 or timothy.holmquist@swri.org.

Sincerely,

Timothy J. Holmquist
Institute Engineer

APPROVED:

James D. Walker

James D. Walker, Ph. D.
Director
Engineering Dynamics Department

Attachments

cc: J. Walker
Record Copy A (Dept. File)
Record Copy B (Contracts)

The Effect of Interface Treatment on Ceramic Performance and Modeling Dyneema® Subjected to Ballistic Impact (Distribution A Version)

Technical Report
SwRI® Report 18.22787/02
PO: 2003301962-Mod 1 (Johns Hopkins University)
Cooperative Agreement No. W911NF-12-2-0022 (Army Research Office)

Prepared by

Timothy J. Holmquist

Southwest Research Institute
5353 Wayzata Boulevard
Suite 607
Minneapolis, MN 55416

Prepared for

Johns Hopkins University
Baltimore, MD 21218

January 23, 2018

DISTRIBUTION STATEMENT A. Approved for public release: distribution unlimited.

Table of Contents

Page

Preface……..viii

1.0 Introduction...1

2.0 The Effect of Interface Treatment on Ceramic Ballistic Performance 3
  2.1 Sphere Impact Onto a Ceramic Target..3
  2.2 The APM2 Impacting Ceramic Plates in the DOP Configuration 10

3.0 Computational Approaches to Model the Ballistic Response of Dyneema®......................15
  3.1 Elastic Orthotropic Material Model and Cohesive Hex Elements.............................15
  3.2 Laminar Composite Material Model 16
  3.3 3D Bar Elements for the Fibers and Solid Elements for the Matrix..........................16
  3.4 Elastic Orthotropic Material Model and Cohesive Wedge Elements 25

4.0 Summary and Conclusions 28

5.0 References...30

List of Figures

Page

Figure 1. Initial geometry for a WC sphere impacting a ceramic plate backed by aluminum..... 4

Figure 2. Computed results for a silicon carbide target impacted by a WC sphere at V = 100 m/s. The results are presented for a target with no bond, and a perfect bond........ 5

Figure 3. Computed results for a silicon carbide target impacted by a WC sphere at V = 200 m/s. The results are presented for a target with no bond, and a perfect bond........ 6

Figure 4. Computed results for a silicon carbide target impacted by a WC sphere at V = 400 m/s. The results are presented for a target with no bond, and a perfect bond. 7

Figure 5. Computed results for a boron carbide target impacted by a WC sphere at V = 100 m/s. The results are presented for a target with no bond, and a perfect bond. 8

Figure 6. Computed results for a boron carbide target impacted by a WC sphere at V = 200 m/s. The results are presented for a target with no bond, and a perfect bond. 9

Figure 7. Computed results for a boron carbide target impacted by a WC sphere at V = 400 m/s. The results are presented for a target with no bond, and a perfect bond. 10

Figure 8. The initial geometry of the APM2 projectile impacting a thin plate of ceramic backed by thick aluminum. 11

Figure 9. Computed results for the APM2 impacting a 2.6 mm SiC plate backed by aluminum. The left shows the results for no bond and the right shows the result for a perfect bond........ 12

Figure 10. Computed results for the APM2 impacting a 5.1 mm SiC plate backed by aluminum. The left shows the results for no bond and the right shows the result for a perfect bond........ 12

Figure 11. Computed results for the APM2 impacting a 2.6 mm boron carbide plate backed by aluminum. The left shows the results for no bond and the right shows the result for a perfect bond. 13

Figure 12. Computed results for the APM2 impacting a 5.1 mm boron carbide plate backed by aluminum. The left shows the results for no bond and the right shows the result for a perfect bond. 13

Figure 13. Computed result demonstrating severe hourglassing using hexahedral elements for large deformation computations. 15

Figure 14. The stress-strain response of SK76 fiber [9] and the model used. The red line is an estimate of the fiber behavior used for the model... 18

Figure 15. Initial geometry for a steel sphere impacting an HB80 Dyneema® panel including the mesh resolution used.. 18

Figure 16. Computed back-face deflection as a function of time for four mesh resolutions. 19

Figure 17. Computed penetration and panel deflection at t = 100, 200, 300, 400, 600, and 1000 μs after impact (V = 441 m/s).. 19

Figure 18. Enlarged view of the computed penetration and panel deflection at t = 200 μs after impact (V = 441 m/s).. 20

Figure 19. Computed deflection at t = 800 μs. The left presents back surface deflection contours measured from the front surface and the right presents a comparison of the computed and experimental penetration channel and remaining thickness of the panel............. 20

Figure 20. Comparison of the computed and experimental back face deflection along the plane of symmetry at t = 400 μs.. 21

Figure 21. Computed penetration and panel deflection at t = 100, 200, 300, 400, 600, and 1000 μs after impact, for an impact velocity of V = 293 m/s)................................... 21

Figure 22. Comparison of the computed and experimental penetration channel at t = 1000 μs after impact, for an impact velocity of V = 293 m/s... 22

Figure 23. Comparison of the computed and experimental back-face deflections for an impact velocity of V = 293 and 441 m/s.. 22

Figure 24. Initial geometry for the 7.9 mm thick panel including the mesh. 23

Figure 25. Computed results for the 7.9 mm thick panel. The panel stops the FSP at V = 1.0 and perforates the panel at V = 1.015. The computed ballistic limit is estimated to be V = 1.008. 24

Figure 26. Initial geometry for the 8.9 mm thick panel including the mesh. 24

Figure 27. Computed results for the 8.9 mm thick panel. The panel stops the FSP at V = 1.079 and perforates the panel at V = 1.088. The computed ballistic limit is estimated to be V = 1.082. 24

Figure 28. Initial geometry for the 10.9 mm thick panel including the mesh. 25

Figure 29. Computed results for the 10.9 mm thick panel. The panel stops the FSP at V = 1.155 and perforates the panel at V = 1.168. The computed ballistic limit is estimated to be V = 1.161. 25

Figure 30. Initial geometry, and the mesh, for the back-face deformation (BFD) configuration. Four layers of symmetric brick elements are joined together by three layers of cohesive wedge elements. 25

Figure 31. Computed result for a sphere impacting a Dyneema panel at V = 441 m/s. The sphere is stopped in the target producing significant delamination. 25

Figure 32. Computed result for a sphere impacting a Dyneema panel at V = 600 m/s. The sphere perforates the target producing significant delamination... 25

PREFACE

This work was performed for Johns Hopkins University under PO: 2003301962-Mod 1 with funding provided by the Army Research Laboratory (ARL). The Author would like to thank Dr. Andrew Tonge and Dr. Richard Becker, from the ARL, for their contributions to this work. This report is a modified version of a limited distribution report submitted to the ARL December 29, 2017. This modified version has been approved for public release by the ARL; there are no limitations on its distribution.

1.0 Introduction

This work documents two separate studies: one that evaluates the effect material interfaces have on the ballistic response of ceramics; and one that evaluates numerical approaches to model the composite Dyneema®. The first study uses several configurations where a ceramic is attached to a metal backing plate and the effect of bonding the plate to the substrate is evaluated. Two material models are used in this study, the Tonge-Ramesh (TR) ceramic model and the Johnson-Holmquist-Beissel (JHB) ceramic model. In the second study several approaches are used to evaluate the ability to model the ballistic response of Dyneema®. Experimental ballistic data were provided by the Army Research Laboratory (ARL) and are used to evaluate the numerical approaches. All the work presented herein use a prerelease of the 2017 Beta version of the EPIC code.

The remainder of this report presents the results for the bonding study followed by a discussion on modeling Dyneema®.

2.0 Effect of Interface Treatment on Ceramic Ballistic Performance

This section presents the results of a computational study that investigates the treatment of interfaces and their effect on the ballistic response of ceramics. Typical ceramic armor is comprised of a ceramic top plate bonded to a substrate (the interface). The objective of this work is to determine how much, and under what conditions, the numerical treatment of the interface influences the results. The approach uses two target configurations, two different projectiles, two different ceramic materials, and two different ceramic models. All the targets are comprised of a ceramic top plate and an aluminum substrate and are computed using a perfect bond (the ceramic and aluminum share nodes) and no bond (the ceramic and aluminum do not share nodes and friction is neglected). The two ceramics investigated are silicon carbide and boron carbide. The silicon carbide is modeled using the Johnson-Holmquist-Beissel (JHB) ceramic model with constants determined in 2005 [1] (EPIC material library #166). The boron carbide is modeled using the Tonge-Ramesh (TR) ceramic model using a recently revised model (TR Version 2016-09-23-133945) and constants, (EPIC material library #149). It should be noted that the revised TR model and constants were incorporated into the EPIC code under this effort and are now the standard. All the computed results are performed in three dimensions with a plane of symmetry, and use a prerelease of the 2017 Beta version of the EPIC code.

2.1 Sphere Impact Onto a Ceramic Target

Figure 1 presents the initial geometry of a tungsten carbide sphere impacting a target consisting of a 6.35 mm thick ceramic plate backed by a 6.35 mm aluminum plate. The sphere is tungsten carbide (0.96WC-0.06Co) and is 12.7 mm in diameter. The ceramic plate is 100 mm x 100 mm and is either silicon carbide or boron carbide. The aluminum back plate is 200 mm x 200 mm and the specific form is 6061-T6. The mesh used is considered "fine" shown on the right side in Fig. 1 resulting in 3,758,112 elements for the entire problem. Three impact velocities are investigated, V = 100, 200, and 400 m/s impacting a target with no bond and a target with a perfect bond. The following responses are compared: the damage and failure of the ceramic; the damage and failure of the sphere; the deformation and damage of the aluminum plate; and the time history of the aluminum back surface displacement located directly under the sphere.

Figures 2-4 present the computed results for silicon carbide (using the JHB model), for impact velocities of V = 100, 200 and 400 m/s respectively. The top-left of the figures present the computed result for no bond and the top-right presents the results for a perfect bond. Also shown are the damage in the spheres, and damage on the front and rear of the silicon carbide plates. The lower portion presents a comparison of the damage in the aluminum back plates and the back surface displacements as a function of time. It is clear that the computed results using no bond produce more damage in the ceramic plate and much more displacement of the aluminum back plate.

Figures 5-7 present the computed results for boron carbide (using the TR model), for impact velocities of V = 100, 200, and 400 m/s respectively. Although the damage patterns are much different than those presented for silicon carbide, the trend is similar; there is less damage in the ceramic plates and the displacement of the aluminum plate is less when the interface is bonded.

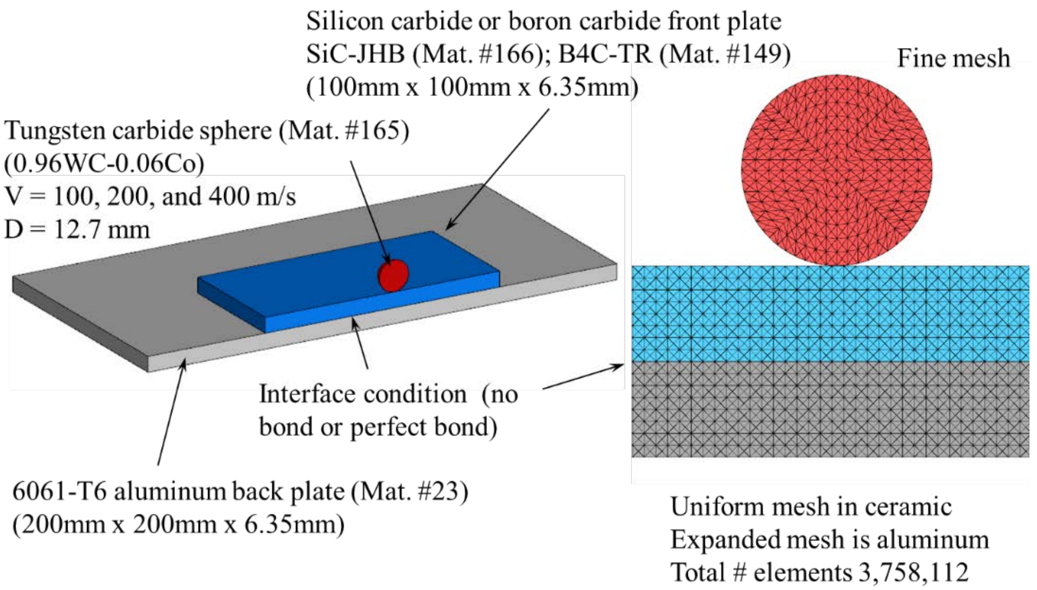
Silicon carbide or boron carbide front plate
SiC-JHB (Mat. #166); B4C-TR (Mat. #149)
(100mm x 100mm x 6.35mm)
Fine mesh
Tungsten carbide sphere (Mat. #165)
(0.96WC-0.06Co)
V = 100, 200, and 400 m/s
D = 12.7 mm
Interface condition (no bond or perfect bond)
6061-T6 aluminum back plate (Mat. #23)
(200mm x 200mm x 6.35mm)
Uniform mesh in ceramic
Expanded mesh is aluminum
Total # elements 3,758,112

Figure 1. Initial geometry for a WC sphere impacting a ceramic plate backed by aluminum.

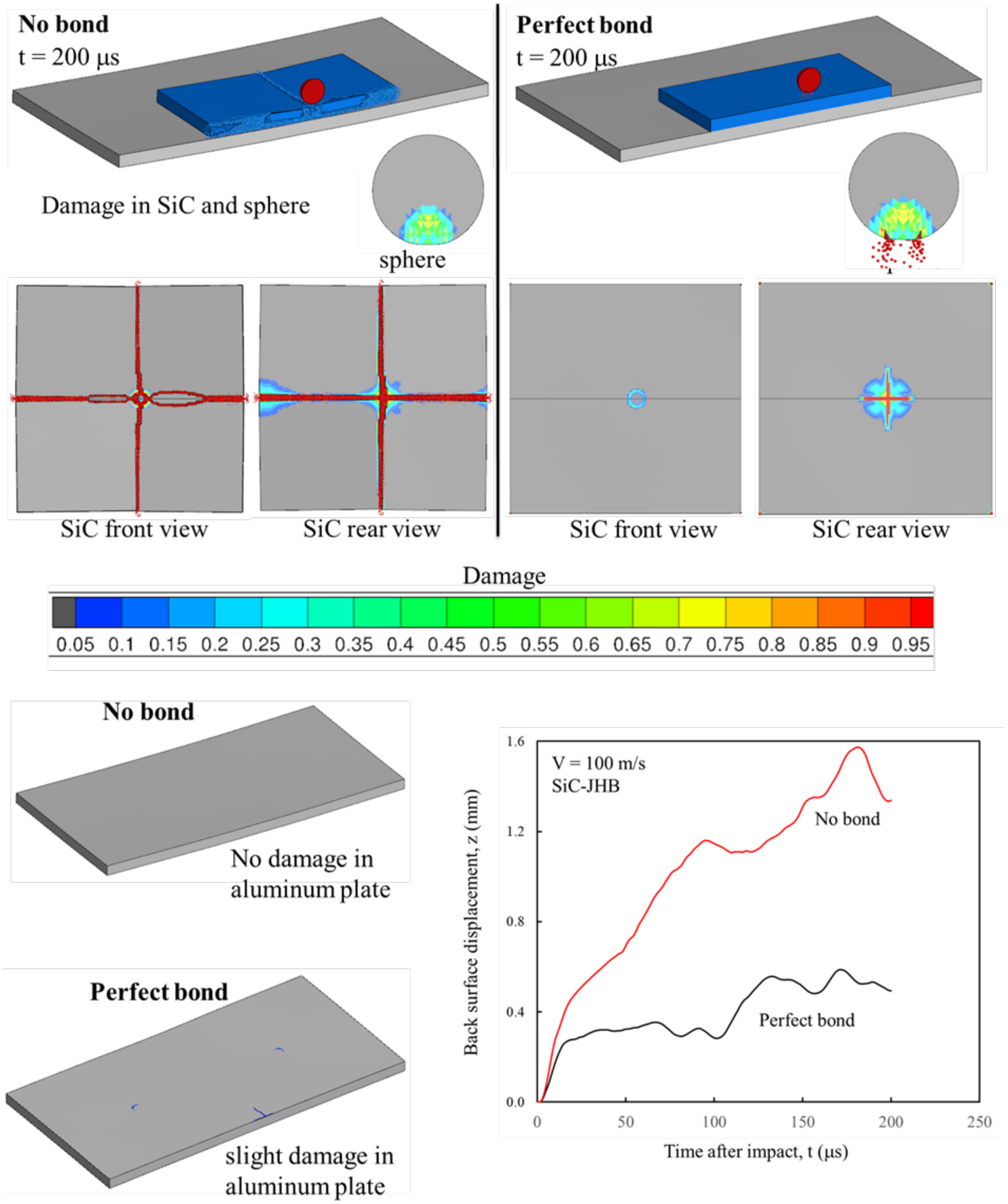

Figure 2. Computed results for a silicon carbide target impacted by a WC sphere at V = 100 m/s. The results are presented for a target with no bond, and a perfect bond.

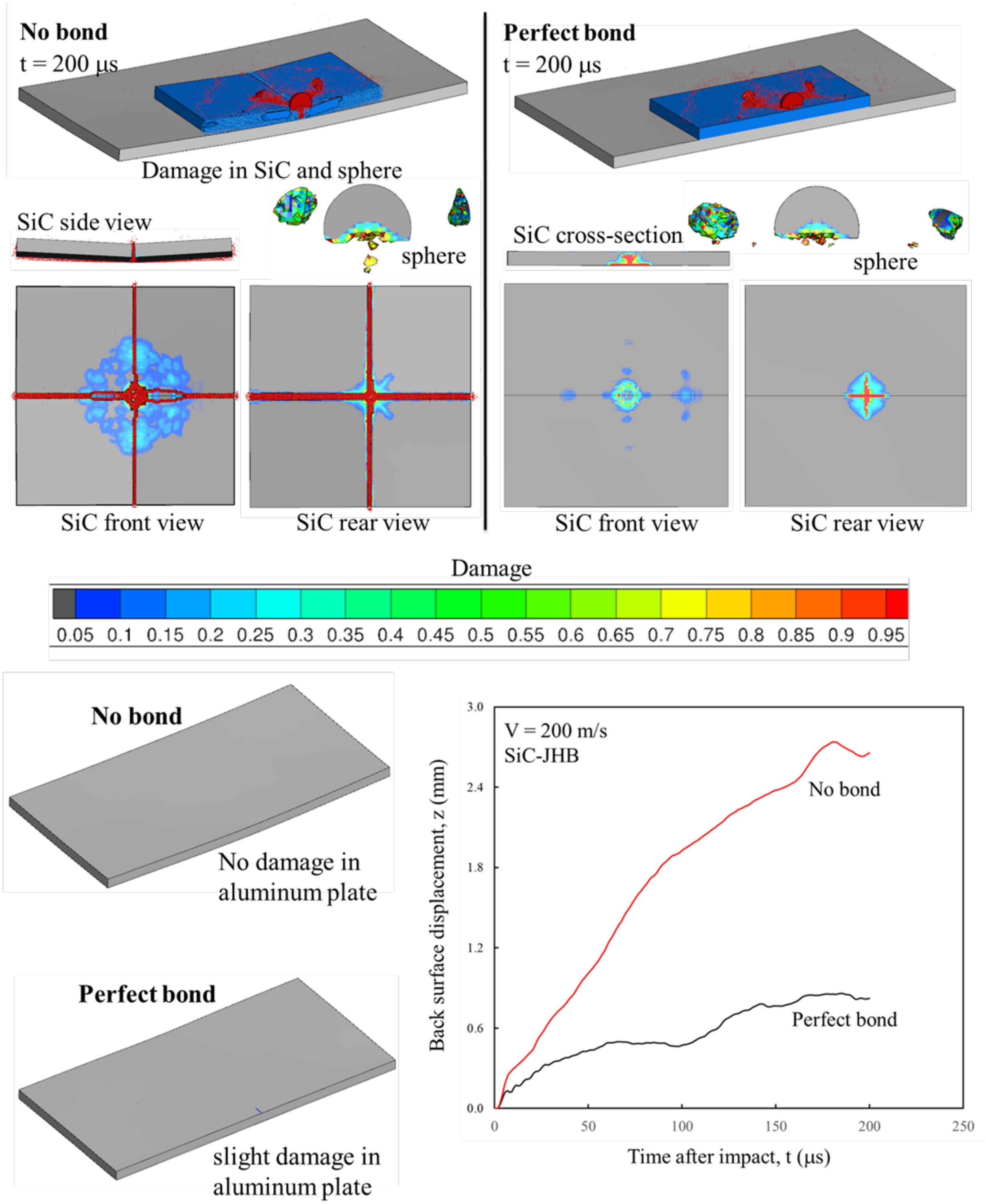

Figure 3. Computed results for a silicon carbide target impacted by a WC sphere at V = 200 m/s. The results are presented for a target with no bond, and a perfect bond.

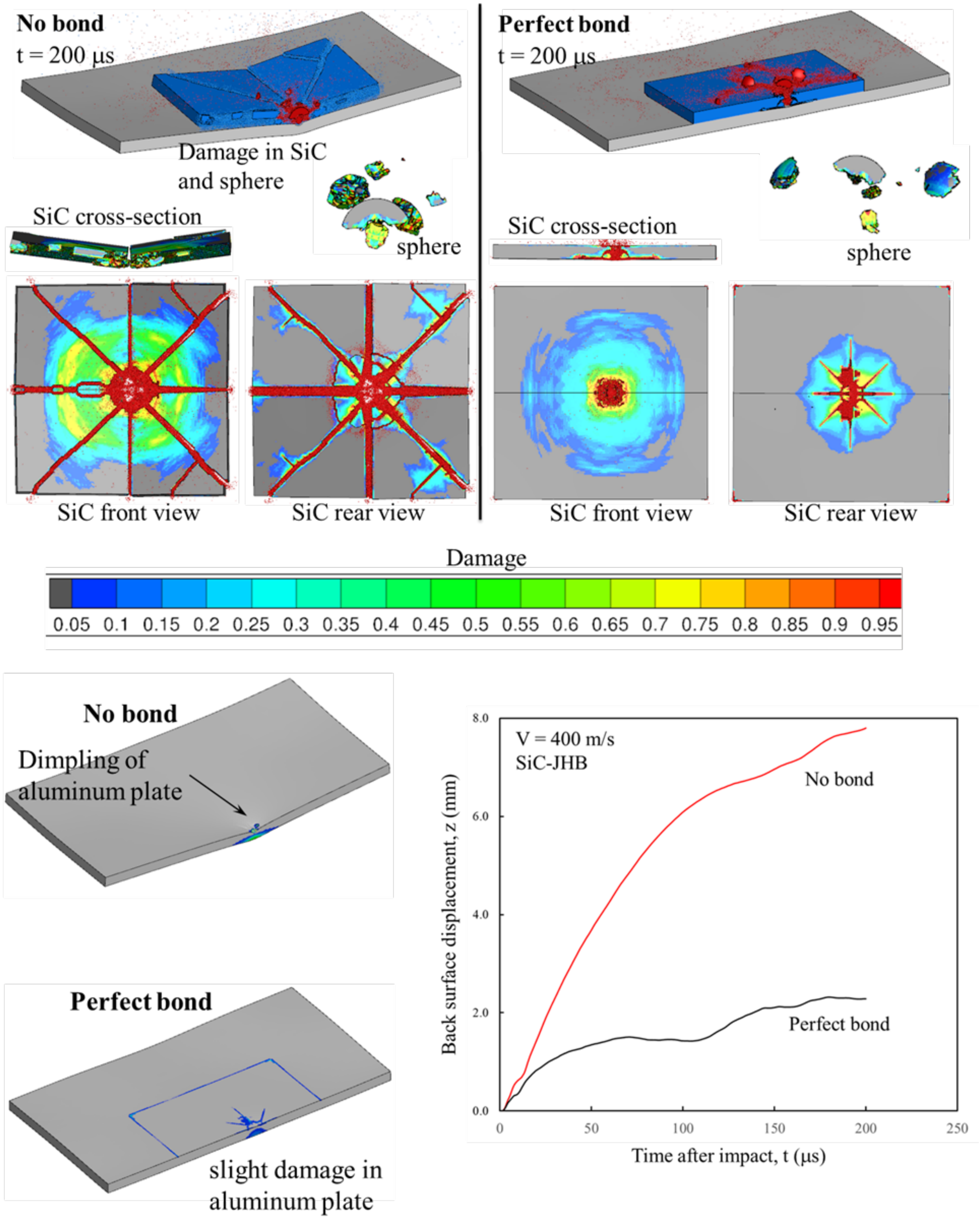

Figure 4. Computed results for a silicon carbide target impacted by a WC sphere at V = 400 m/s. The results are presented for a target with no bond, and a perfect bond.

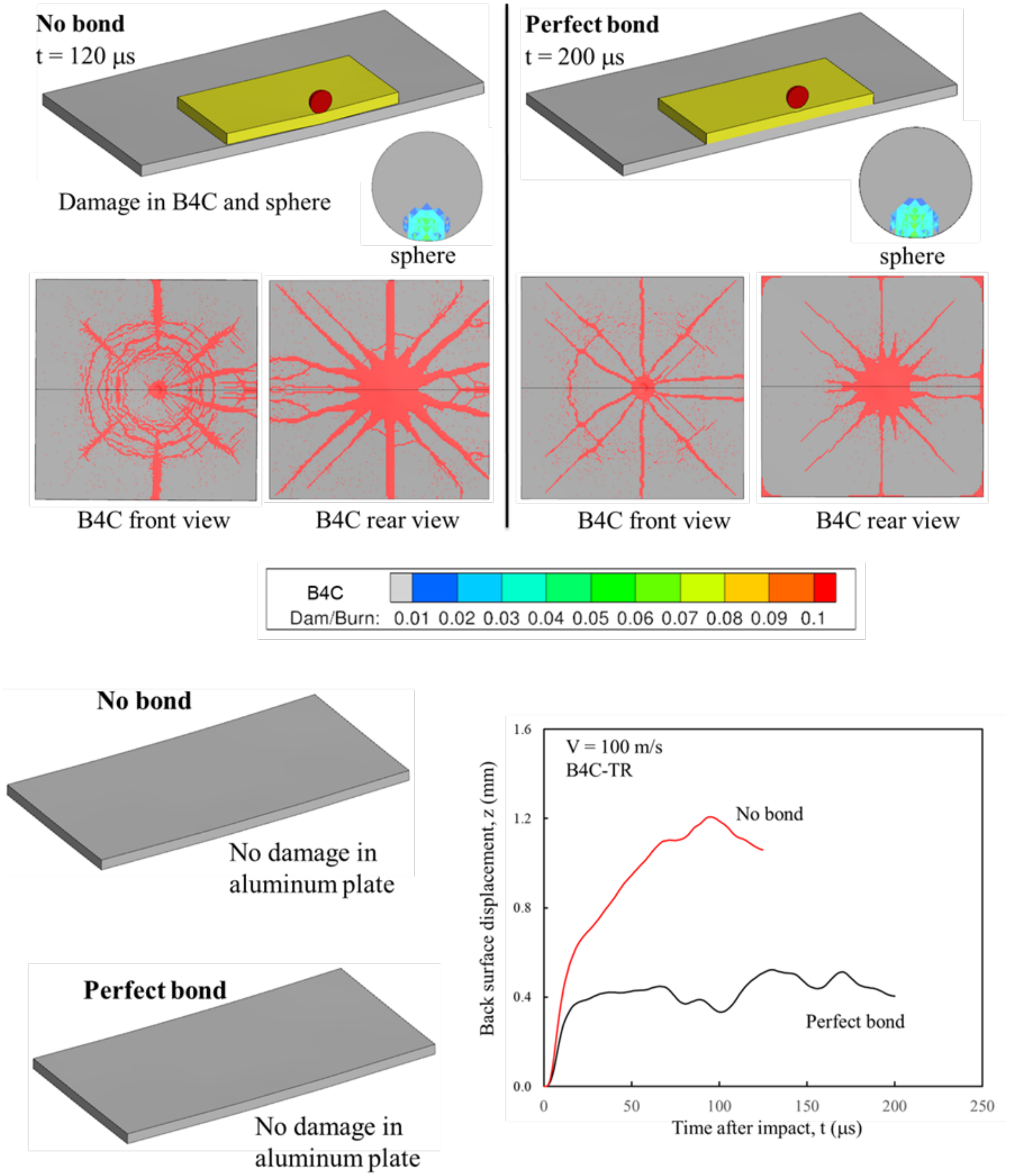

Figure 5. Computed results for a boron carbide target impacted by a WC sphere at V = 100 m/s. The results are presented for a target with no bond, and a perfect bond.

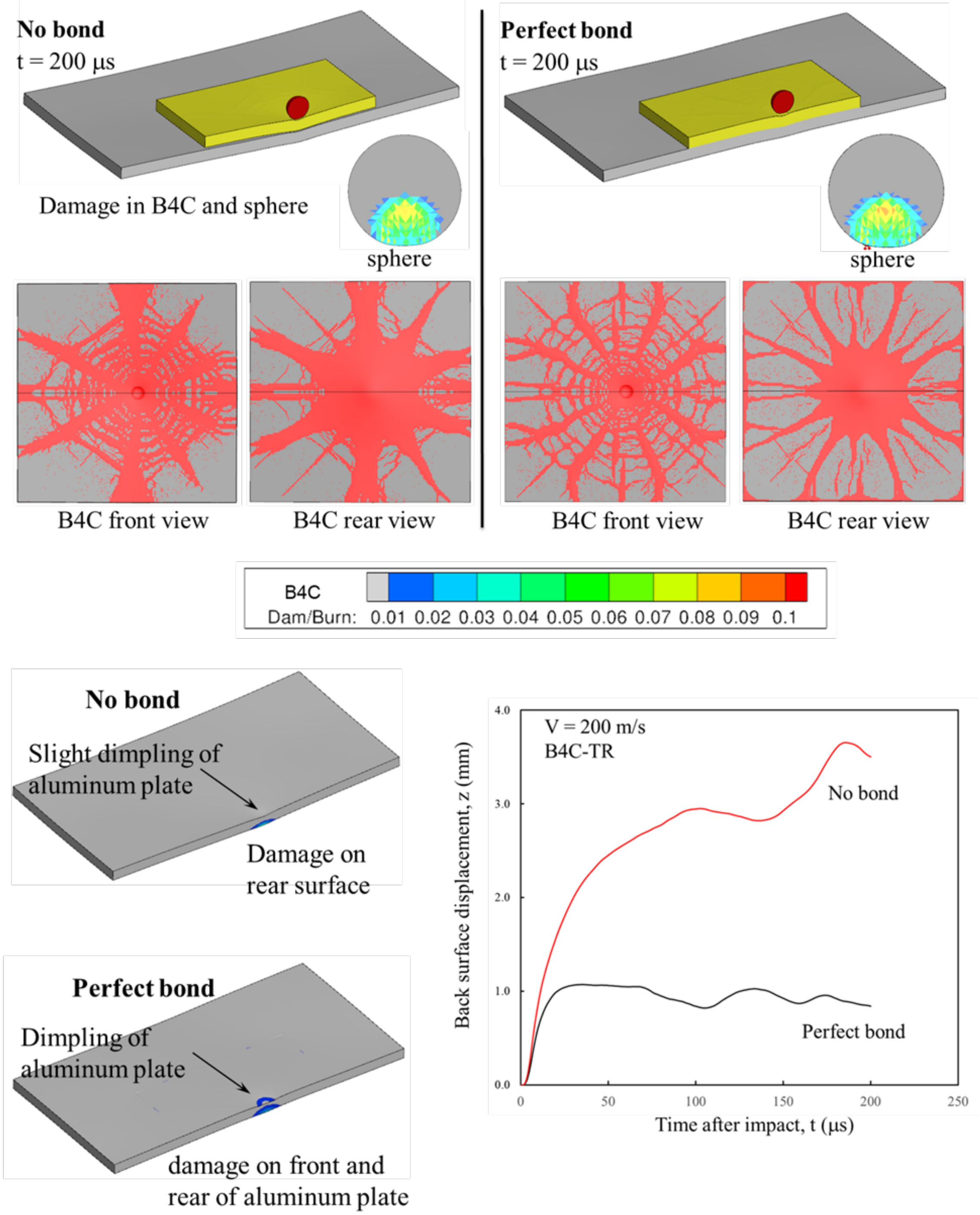

Figure 6. Computed results for a boron carbide target impacted by a WC sphere at V = 200 m/s. The results are presented for a target with no bond, and a perfect bond.

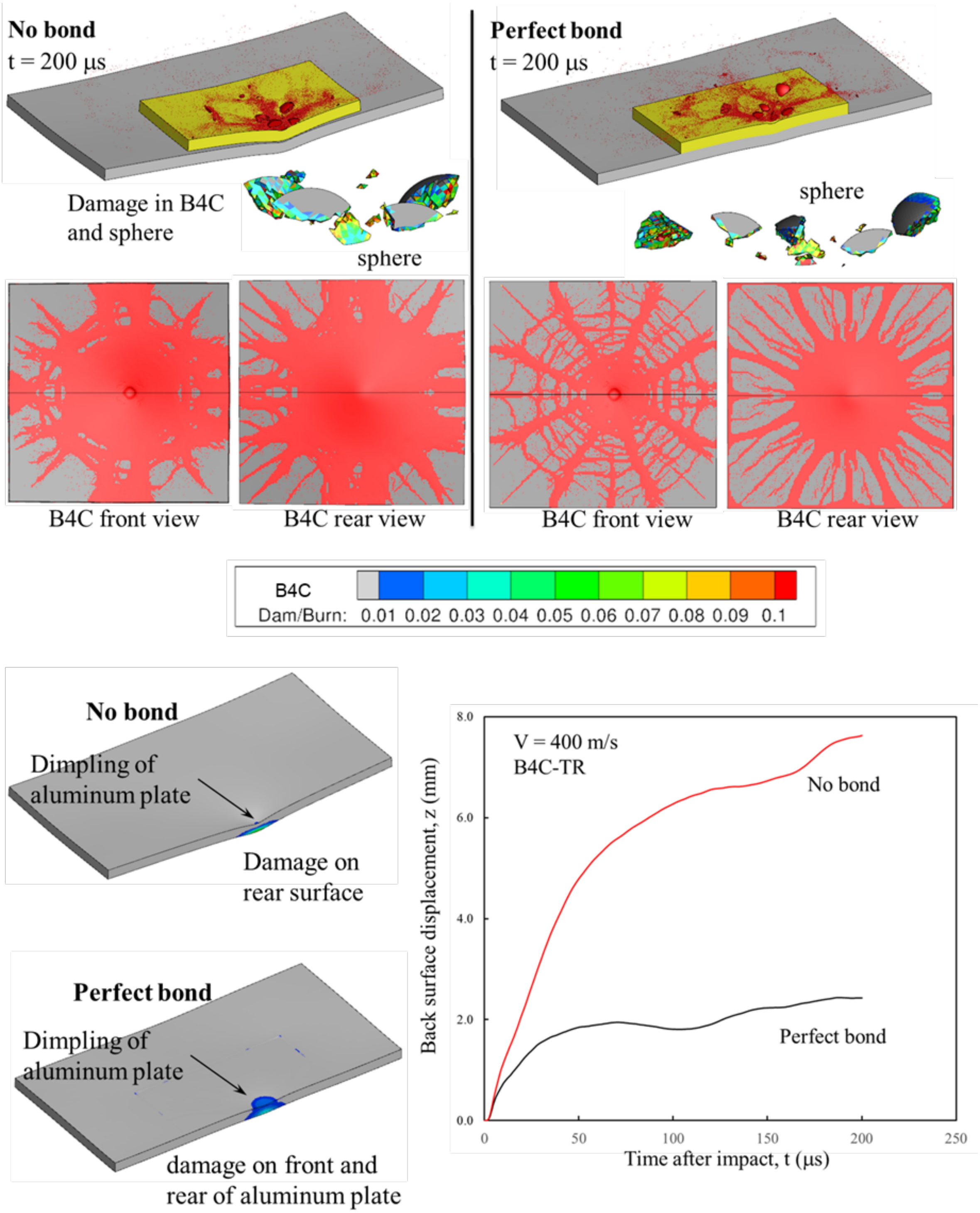

Figure 7. Computed results for a boron carbide target impacted by a WC sphere at V = 400 m/s. The results are presented for a target with no bond, and a perfect bond.

2.2 The APM2 Impacting Ceramic Plates in the DOP Configuration

Figure 8 presents the initial geometry for the 0.30-cal APM2 projectile impacting a ceramic plate backed by thick 5083-H131 aluminum (this is referred to as the Depth-Of-Penetration (DOP) configuration). This geometry, and impact velocity of V = 840 m/s (muzzle) are chosen because there are experimental data available, provided by Moynihan *et al.* [2]. Four thicknesses of silicon carbide and boron carbide (t = 1.25, 2.60, 3.75, and 5.1 mm) were tested and the ceramic was always bonded to the aluminum back plate. The bond was provided by a two-part 24-hour-cure epoxy. The ceramic was pressed onto the face of the aluminum, forcing the epoxy to flow out, leaving a minimal layer of epoxy. It is not known what the strength of the bond was, but generally these bonds are weak relative the joined materials. The experimental results provide the depth of penetration into the aluminum and the condition of the core. They also note that the APM2 jacket and filler are stripped from the core during penetration. Another noteworthy observation is that the ceramics used in the experiments were produced by Cercom (now CoorsTek) denoted SiC-B and PAD B4C, and are the same materials used in determining constants for the JHB and TR models.

Figures 9-12 present the computed results for two thicknesses of silicon carbide and boron carbide (t = 2.6 and 5.1 mm). Figures 9 and 10 present the results for the silicon carbide using the JHB model and Figs. 11 and 12 present the results for the boron carbide using the TR model. Each figure presents the computed results for no bond (left side) and for the perfect bond (right side) including the damage in the ceramic and the projectile core. Also presented are the results of the experiments providing the number of tests, the penetration into the aluminum, and the condition of the core. The results presented in Fig. 9 show very little difference in the depth of penetration and core damage, but there is a large difference in the amount of damage in the silicon carbide. The computed penetration depth is greater than those produced experimentally. The results presented in Fig. 10, where the tile is 5.1 mm thick, show very little penetration with no bond, and no penetration into the aluminum with a perfect bond. The perfect bond also produces more core erosion and less damage in the SiC. The computed results bound the experimental results.

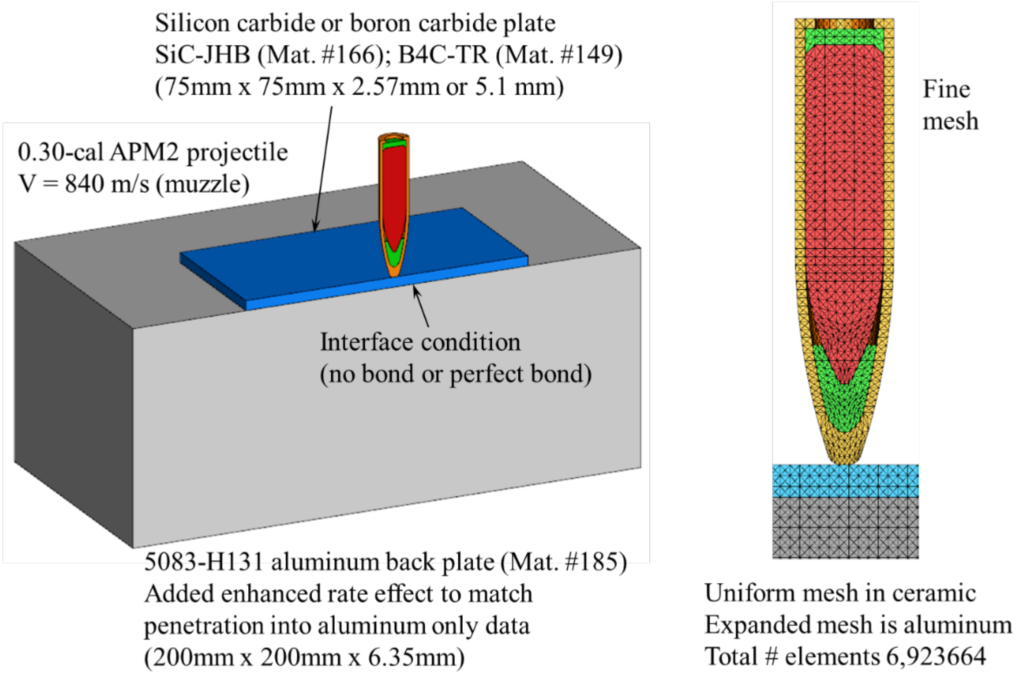
Silicon carbide or boron carbide plate
SiC-JHB (Mat. #166); B4C-TR (Mat. #149)
(75mm x 75mm x 2.57mm or 5.1 mm)
0.30-cal APM2 projectile
V = 840 m/s (muzzle)
Interface condition
(no bond or perfect bond)
5083-H131 aluminum back plate (Mat. #185)
Added enhanced rate effect to match
penetration into aluminum only data
(200mm x 200mm x 6.35mm)
Fine
mesh
Uniform mesh in ceramic
Expanded mesh is aluminum
Total # elements 6,923664

Figure 8. The initial geometry of the APM2 projectile impacting a thin plate of ceramic backed by thick aluminum.

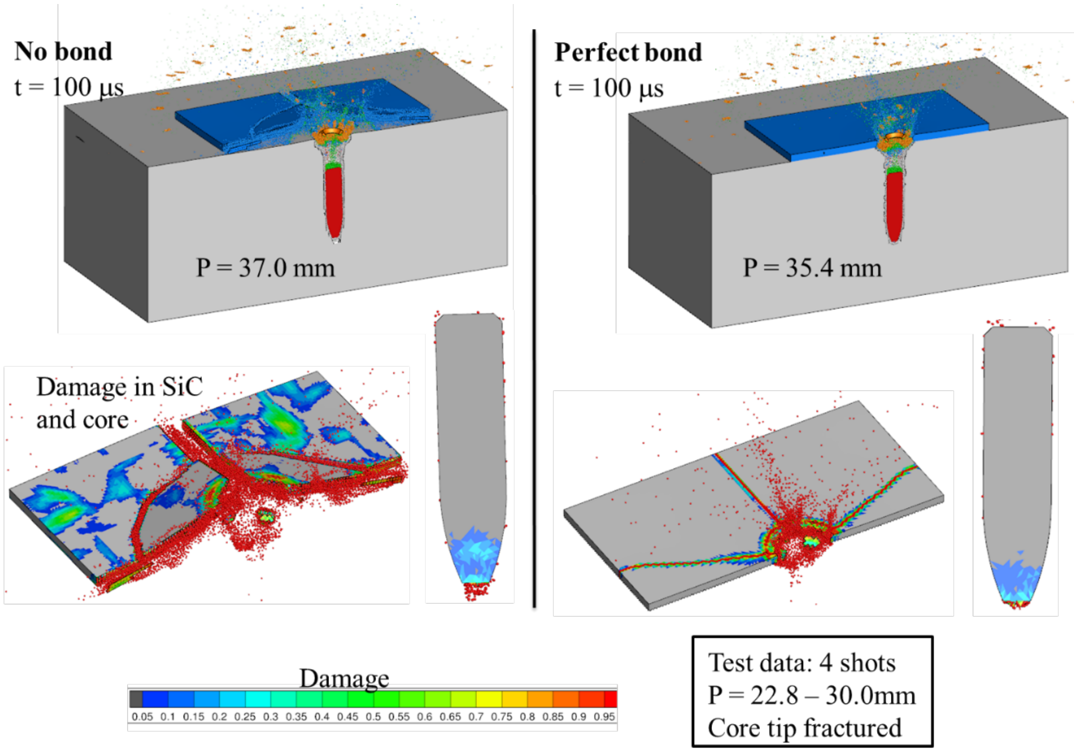
No bond
t = 100 µs
P = 37.0 mm
Damage in SiC
and core
Perfect bond
t = 100 µs
P = 35.4 mm
Damage
0.05 0.1 0.15 0.2 0.25 0.3 0.35 0.4 0.45 0.5 0.55 0.6 0.65 0.7 0.75 0.8 0.85 0.9 0.95

Test data: 4 shots
P = 22.8 – 30.0mm
Core tip fractured

Figure 9. Computed results for the APM2 impacting a 2.6 mm SiC plate backed by aluminum. The left shows the results for no bond and the right shows the results for a perfect bond.

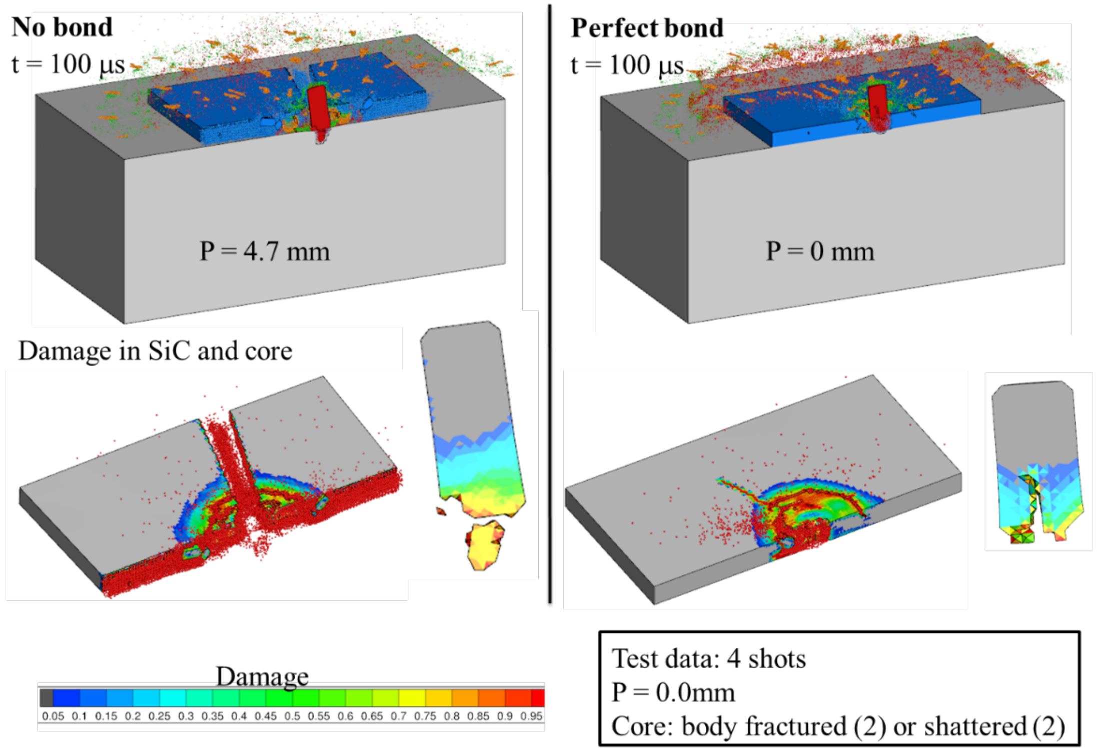
No bond
t = 100 µs
P = 4.7 mm
Damage in SiC and core
Perfect bond
t = 100 µs
P = 0 mm
Damage
0.05 0.1 0.15 0.2 0.25 0.3 0.35 0.4 0.45 0.5 0.55 0.6 0.65 0.7 0.75 0.8 0.85 0.9 0.95

Test data: 4 shots
P = 0.0mm
Core: body fractured (2) or shattered (2)

Figure 10. Computed results for the APM2 impacting a 5.1 mm SiC plate backed by aluminum. The left shows the results for no bond and the right shows the results for a perfect bond.

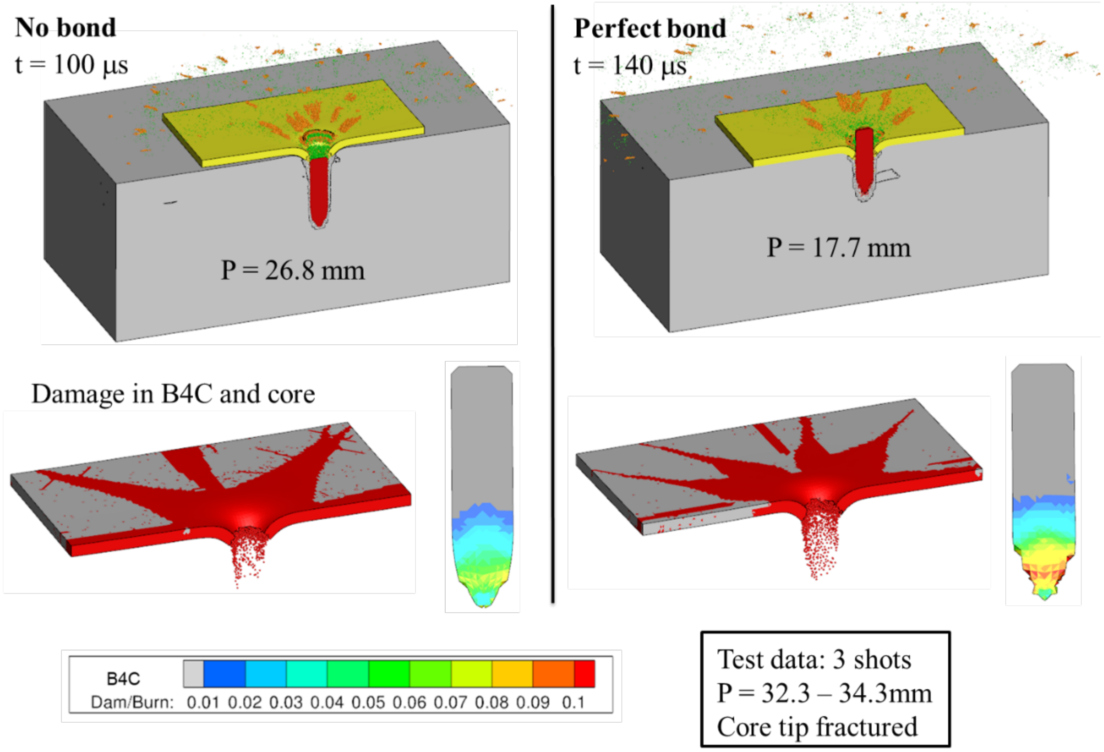
No bond
t = 100 μs
P = 26.8 mm
Perfect bond
t = 140 μs
P = 17.7 mm
Damage in B4C and core
B4C
Dam/Burn: 0.01 0.02 0.03 0.04 0.05 0.06 0.07 0.08 0.09 0.1

Test data: 3 shots
P = 32.3 – 34.3mm
Core tip fractured

Figure 11. Computed results for the APM2 impacting a 2.6 mm boron carbide plate backed by aluminum. The left shows the results for no bond and the right shows the results for a perfect bond.

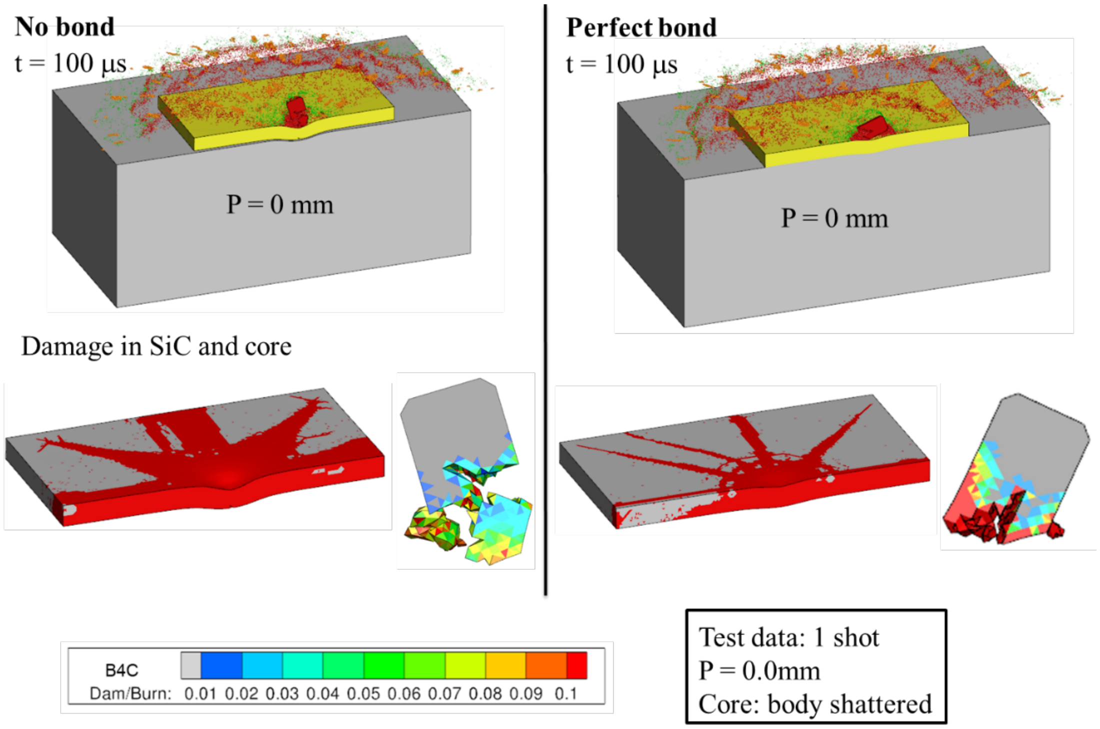
No bond
t = 100 μs
P = 0 mm
Perfect bond
t = 100 μs
P = 0 mm
Damage in SiC and core
B4C
Dam/Burn: 0.01 0.02 0.03 0.04 0.05 0.06 0.07 0.08 0.09 0.1

Test data: 1 shot
P = 0.0mm
Core: body shattered

Figure 12. Computed results for the APM2 impacting a 5.1 mm boron carbide plate backed by aluminum. The left shows the results for no bond and the right shows the results for a perfect bond.

The results presented in Fig. 11, for a 2.6 mm boron carbide tile, show less penetration, more core erosion, and less damage in the ceramic when a perfect bond is used. The computed penetration depths are less than those produced experimentally. The results presented in Fig. 12, for a 5.1 mm tile, show interface defeat and significant core erosion for both bonding conditions; there is slightly less ceramic damage for a perfect bond. The computed results are in agreement with the experimental result inasmuch as there is no penetration into the aluminum.

3.0 Computational Approaches to Model the Ballistic Response of Dyneema®

This section presents computational approaches to model the ballistic response of the composite Dyneema®. The approaches include: hexahedral elements using an elastic orthotropic material model and cohesive elements; a new laminar material model developed at SwRI [3]; 3D bar elements to represent the fibers and solid elements to represent the matrix; and tetrahedral elements (in a symmetric brick arrangement) using an elastic orthotropic material model and cohesive wedge elements. Each approach will be discussed in turn.

3.1 Elastic Orthotropic Material Model and Cohesive Elements

This work was performed by the ARL (Jason McDonald), in collaboration with SwRI. The approach used hexahedral elements to describe the response of the fibers and matrix (using an orthotropic elastic material model), and cohesive elements to model the delamination. This was the approach used by Zhang *et al.* [4] to model Dyneema® using LS-DYNA. In the 2016 version of EPIC, cohesive elements can only be used to attach hexahedral elements and this is why this element type was used for this study. This approach was determined to be infeasible because the large deformations resulted in severe hourglassing and contact issues (as shown in Fig. 13) resulting in numerical instability. Because the symmetric brick arrangement (24 tetrahedral elements arranged in a symmetric brick configuration) is much more robust, and is the recommended element type for severe distortions in EPIC, the hexahedral approach was abandoned. Recently, with funding under a different contract, cohesive wedge elements were added to EPIC. This new feature allows symmetric brick elements to be attached using cohesive wedge elements, no longer requiring hexes to be used. This approach will be discussed later in this section.

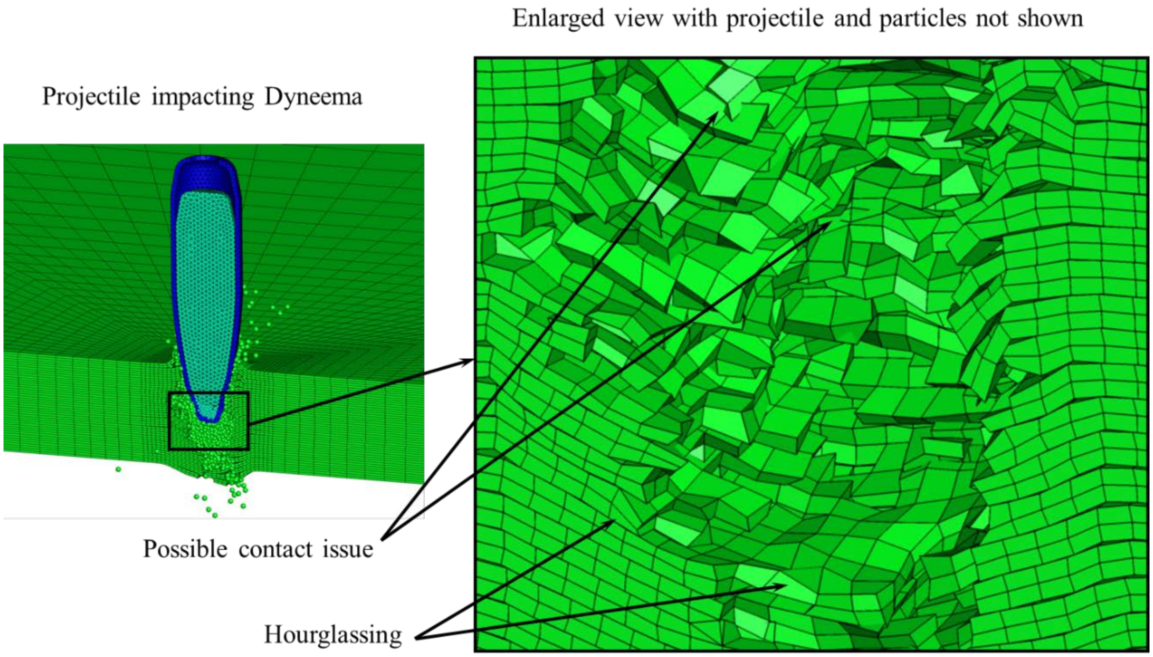
Enlarged view with projectile and particles not shown
Projectile impacting Dyneema
Possible contact issue
Hourglassing

Figure 13. Computed result demonstrating severe hourglassing using hexahedral elements for large deformation computations.

3.2 Laminar Composite Material Model

A new material model was recently developed at SwRI [3] and incorporated into EPIC [5]. This model was developed to simulate composite materials and account for high strength fibers, the matrix material, and several failure modes. The advantage of the model is that it is a material model where the material input is straightforward needing only the elastic constants of the constituents; it also has the ability to include different fiber orientations. This model was used to model Dyneema® in EPIC, but was not robust in its current form. It was found that instabilities occur when the model fails material and reduces some components of the elastic constants in the matrix material to very small values. A solution to these instabilities was identified and implemented into the 2017 Beta version of EPIC (under different funding), but there was not sufficient time to evaluate this approach for this study. This approach has the possibility to be a very good option to model Dyneema®.

3.3 3D Bar Elements for the Fibers and Solid Elements for the Matrix

This approach uses 3D bar elements to represent the fibers and 3D solid elements to represent the matrix material. This approach was originally developed by Johnson *et al.* [6] and it has been successfully used to model composites in the past. The advantage of this approach is the orthogonal fibers are modeled explicitly with bar elements using published material properties for the fibers; it is also efficient and robust. The disadvantage is that the solid elements that represent the matrix occupy all of the volume requiring the matrix material properties (density, stiffness, and strength) to be artificially reduced to account for the added volume (a more thorough discussion is provided by Johnson *et al.* [6]). The specific approach used here, to model the ballistic response of Dyneema®, uses published material behavior for the fibers, and estimated constants for the matrix. The matrix material is modeled using the Johnson-Cook models that are simplified to an elastic-perfectly plastic strength, and a constant failure strain. This simple model requires only the elastic constants (density and stiffness), the flow stress, and the failure strain. The density is known so the stiffness, flow stress and failure strain are estimated from laboratory data, and by performing computations of ballistic impact experiments using values that produce results that are in good agreement with the tests. The following presents the approach used to model Dyneema® using bars and elements.

The specific Dyneema® panel modeled here is HB80 comprised of SK76 fibers and matrix (resin). The fibers account for nominally 80% of the volume and the resin accounts for the remaining 20%. Both the fiber and resin have a density of 980 kg/m^3. Figure 14 presents the test data and model used for SK76 fibers. The test data are provided by Russell *et al.* [7] where the stress-strain responses are presented for yarn and single fiber; the test data are shown to failure. The nominal fiber behavior is represented by the red line and has a young's modulus of 90 GPa, a maximum strength of 3.8 GPa, and a plastic strain to failure of 0.01. The model used to represent the fibers is shown on the right. This model was originally developed by Johnson, Beissel, and Cunniff to model fabrics (referred to as the JBC fabric model) and this is why there are two stiffness provided; E_1 represents the slack, or crimp, in the fabric, and E_2 represents the stiffness when the slack has been removed. This model can readily be used to model the SK76 fiber by setting E_1 = 89 GPa, E_2 = 90 GPa (a requirement of the model is that E_1 must be less than E_2), density = 980 kg/m^3, ε_{lock} = 0.001, σ_{max} = 3.8 GPa, and ε_{max} = 0.01 (here ε_{max} is the plastic strain to failure).

Ballistic experiments, using HB80 panels, are provided by Zhang *et al.* [8] and are used here to evaluate the approach, and help determine the matrix behavior. They include the normalized ballistic limit (V_{50}) for three areal densities of HB80, (AD = 7.8, 8.8, and 10.7 kg/m^2) impacted by

0.22-cal fragment simulating projectiles (FSP), and the ballistic response of a 7.8 kg/m^2 HB80 panel impacted by a steel sphere. Because the behavior of the matrix material within the HB80 panel is difficult to determine, it was decided to use computations to help determine its response. Computations of the test data provided by Zhang *et al.* were performed using variations in matrix material parameters provided by Holmquist [9] in 2014. Johnson-Cook strength and failure model constants, and the stiffness, were determined by producing computed results that were in good agreement with the experiments. These are the same constants provided by Holmquist [9] with the exception of the stiffness which was increased. Although the stiffness was increased significantly, it still appears reasonable, relative to what is available in the literature [10-12]. Figures 15-29 present the computed results and a comparison to the experiments for the three FSP configurations, and the two sphere impact configurations. All the computed results use the same set of constants. The sphere impact configuration will be discussed first followed by the V_{50} configuration.

Figure 15 presents the initial geometry for the sphere impact configuration including the mesh resolution used. The HB80 Dyneema® panel is 300 mm square and 7.9 mm thick. The steel sphere is 12.7 mm in diameter and impacts the panel at V = 441 m/s (test 458A-1) and at V = 293 m/s (test 545A). Digital image correlation (DIC) was used to measure the displacement of the back surface as a function of time. Computed tomography (CT) scans of the post-mortem panels were also performed to determine final penetration into the panels and the magnitude of delamination. As shown in Fig. 15, six layers of elements, through the plate thickness, were used as this resolution produced a converged solution as shown in Fig. 16. Figure 16 presents the maximum back-face deflection (BFD) as a function of time for four mesh resolutions. The BFD for 6 and 7 elements are very similar indicating convergence. All the BFD computations presented herein use 6 elements through the panel thickness and a uniform mesh throughout the entire panel resulting in 1,377,501 elements used. The computations were computed to t = 1000 μs requiring approximately 1.5 hours to complete using 16 processors.

Figures 17-20 present the computed results for an impact velocity of V = 441 m/s. Figure 17 shows sphere penetration and panel deformation at t = 100, 200, 300, 400, 600, and 1000 μs after impact. The maximum computed BFD is 27.0 mm and occurs approximately 400 μs after impact. Figure 18 presents an enlarged view of the penetration, delamination, and deflection of the back surface at t = 200 μs. Delamination occurs naturally and is a result of matrix failure. Figure 19 presents back face deflection contours and panel penetration at t = 800 m/s after impact. The deflection contours show the typical diamond pattern similar to the experiment. The computed maximum BFD = 27.0 mm is in reasonable agreement with the experimental value of 28.7 mm. The computed remaining thickness is approximately 29% (determined by how many fiber layers are remaining: 2/7, this was used because most of the mass is represented by the fibers) less than the 40.3% remaining experimentally. Figure 20 presents a comparison of the computed and experimental BFD along the plane of symmetry at t = 400 μs. The computed deformation is slightly less than the experiment.

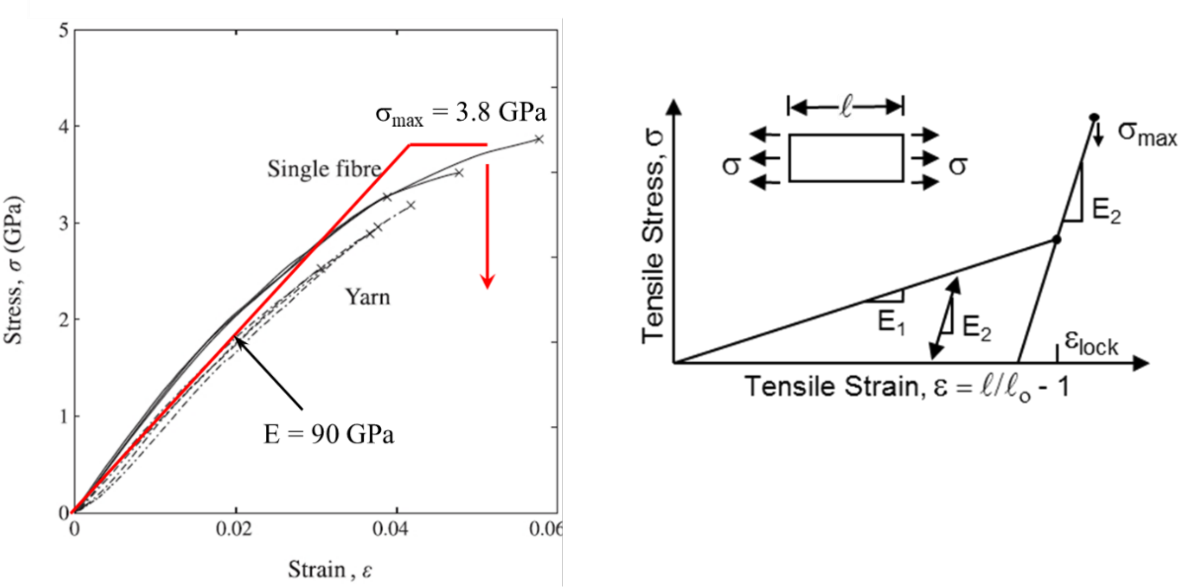

Figure 14. The stress-strain response of SK76 fiber [7] and the model used. The red line is an estimate of the fiber behavior used for the model.

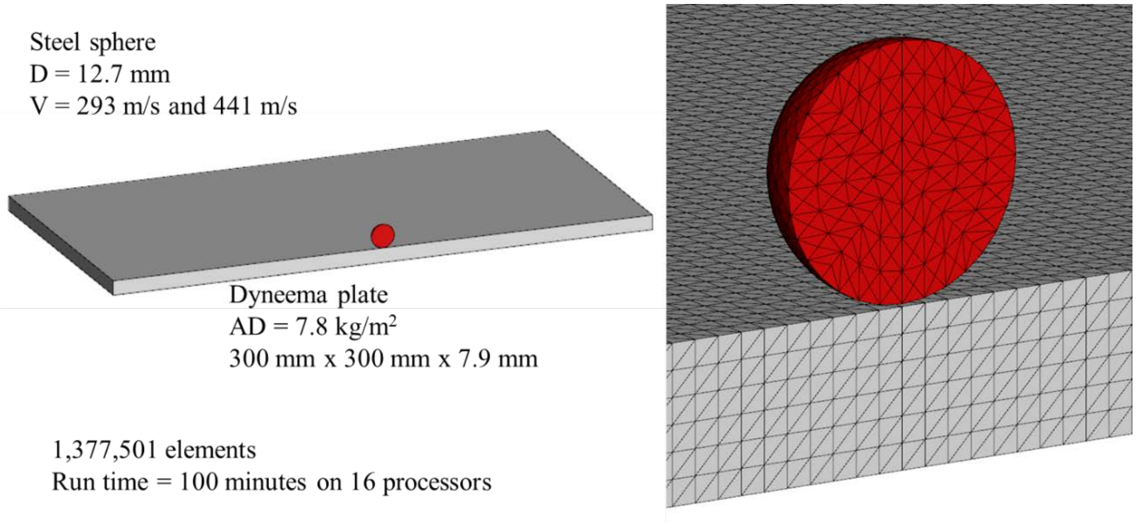

Steel sphere
D = 12.7 mm
V = 293 m/s and 441 m/s

Dyneema plate
AD = 7.8 kg/m^2
300 mm x 300 mm x 7.9 mm

1,377,501 elements
Run time = 100 minutes on 16 processors

Figure 15. Initial geometry for a steel sphere impacting an HB80 Dyneema® panel including the mesh resolution used.

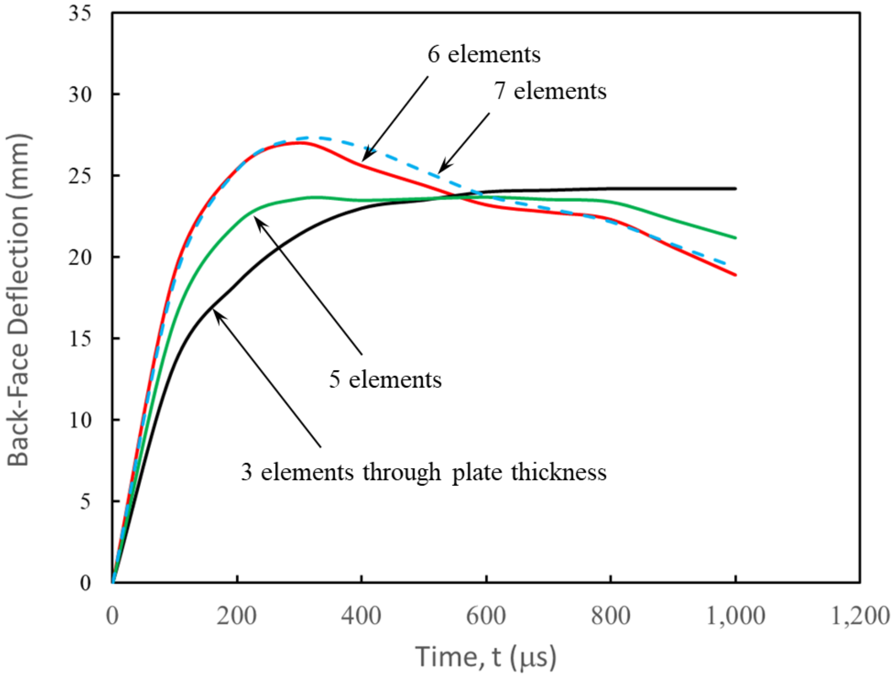

Figure 16. Computed back-face deflection as a function of time for four mesh resolutions.

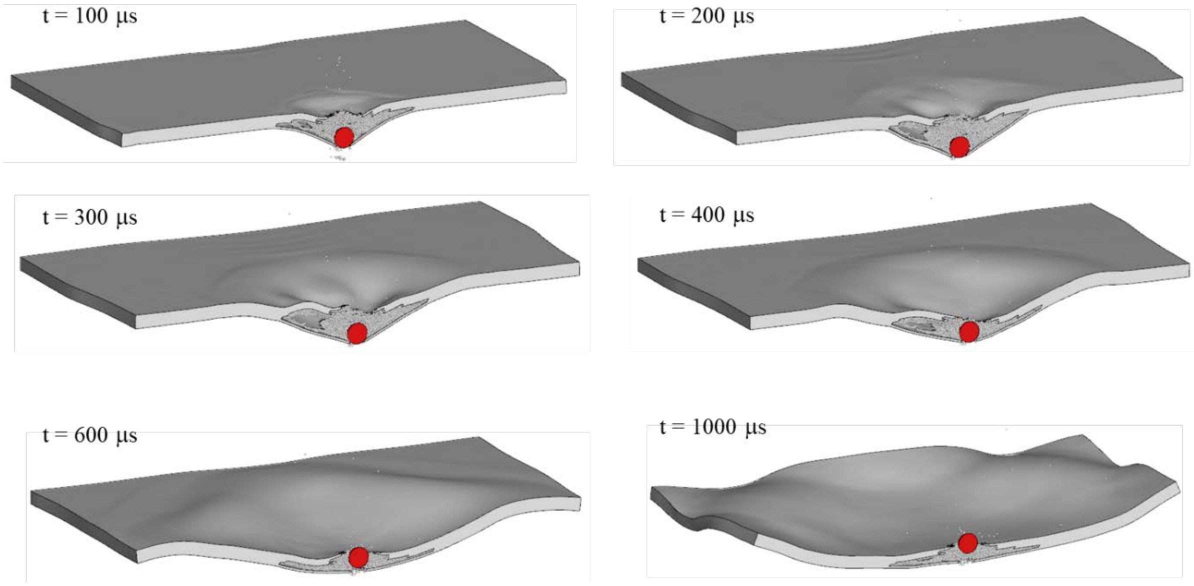
t = 100 μs
t = 200 μs
t = 300 μs
t = 400 μs
t = 600 μs
t = 1000 μs

Figure 17. Computed penetration and panel deflection at t = 100, 200, 300, 400, 600, and 1000 μs after impact (V = 441 m/s).

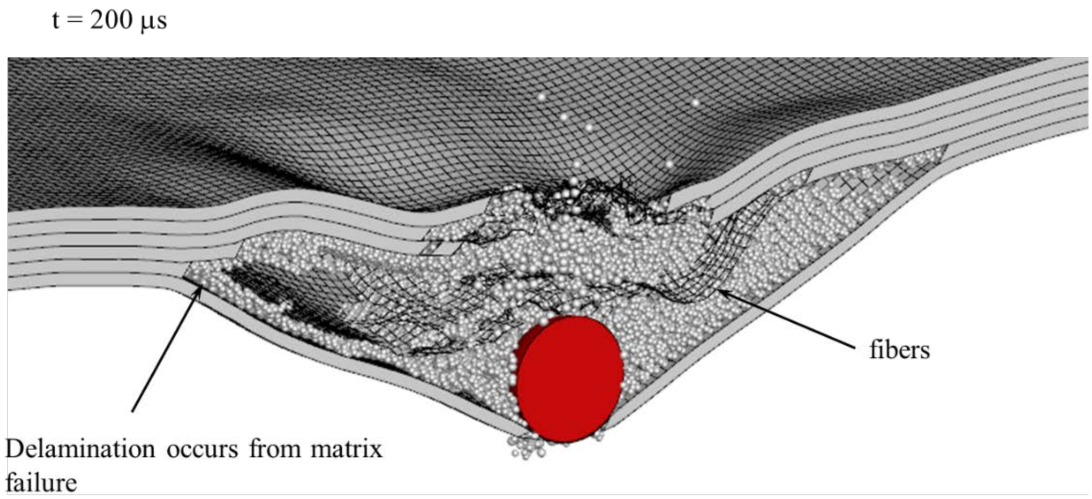
t = 200 μs
fibers
Delamination occurs from matrix failure

Figure 18. Enlarged view of the computed penetration and panel deflection at t = 200 μs after impact (V = 441 m/s).

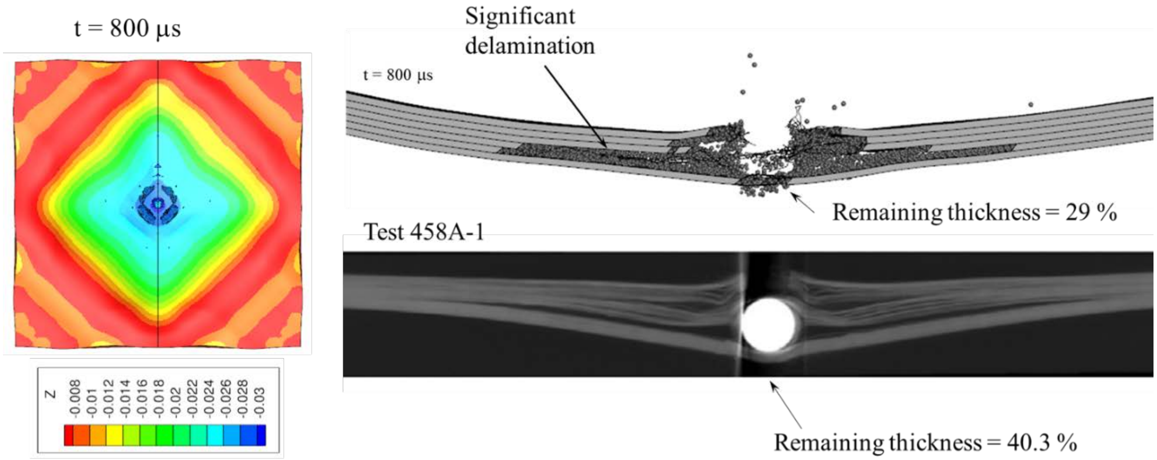
t = 800 μs
Z
-0.008
-0.01
-0.012
-0.014
-0.016
-0.018
-0.02
-0.022
-0.024
-0.026
-0.028
-0.03
Significant delamination
t = 800 μs
Remaining thickness = 29 %
Test 458A-1
Remaining thickness = 40.3 %

Figure 19. Computed deflection at t = 800 μs. The left presents back surface deflection contours measured from the front surface and the right presents a comparison of the computed and experimental penetration channel and remaining thickness of the panel.

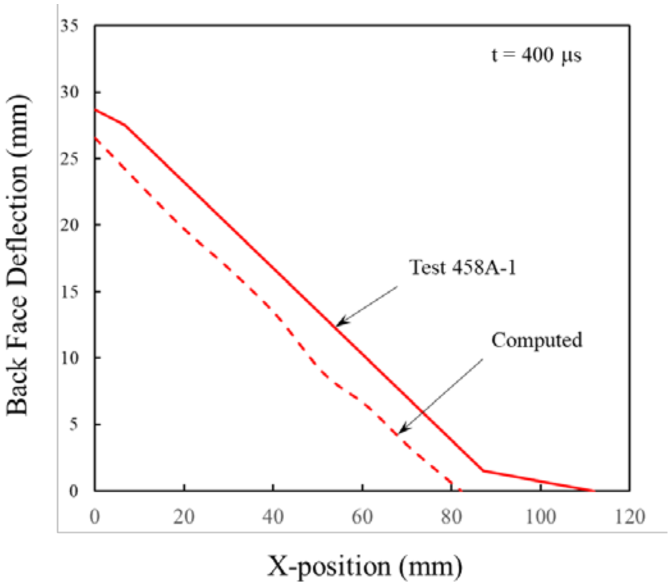

Figure 20. Comparison of the computed and experimental back face deflection along the plane of symmetry at t = 400 μs.

Figures 21 and 22 present the BFD computed results for an impact velocity of V = 293 m/s. Figure 21 shows sphere penetration and panel deformation at t = 100, 200, 300, 400, 600, and 1000 μs after impact. The maximum BFD is 17.5 mm and occurs approximately 800 μs after impact in reasonable agreement with the experimental value of 16.3 mm. Figure 22 presents a comparison of the computed and experimental penetration channels. The computed remaining thickness is approximately 71% (determined by how many fiber layers are remaining: 5/7), less than the 76.4% remaining experimentally. Lastly, Fig. 23 presents a comparison of the computed and experimental back-face deflection time histories for the two impact velocities.

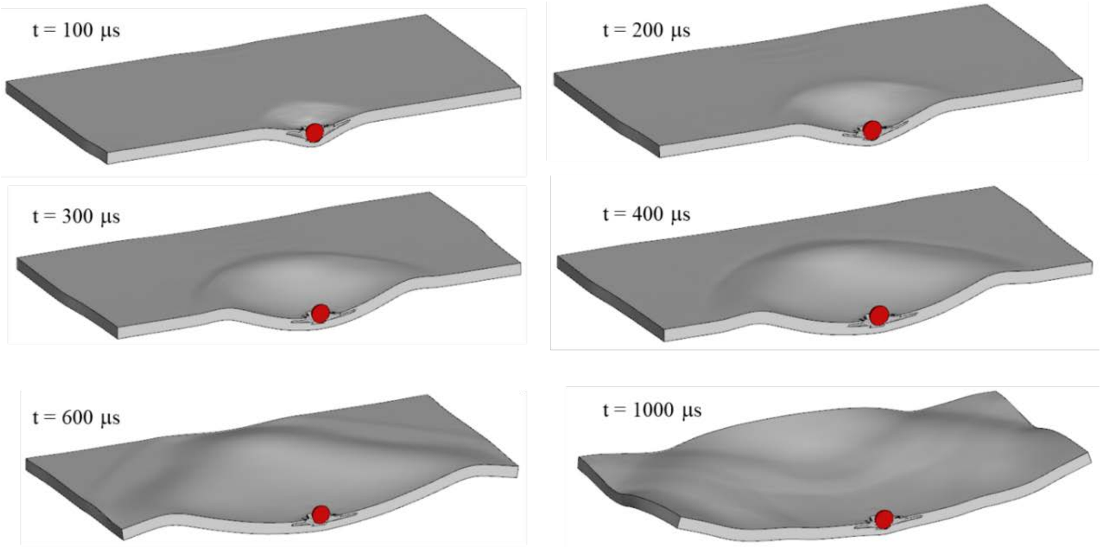

Figure 21. Computed penetration and panel deflection at t = 100, 200, 300, 400, 600, and 1000 μs after impact, for an impact velocity of V = 293 m/s).

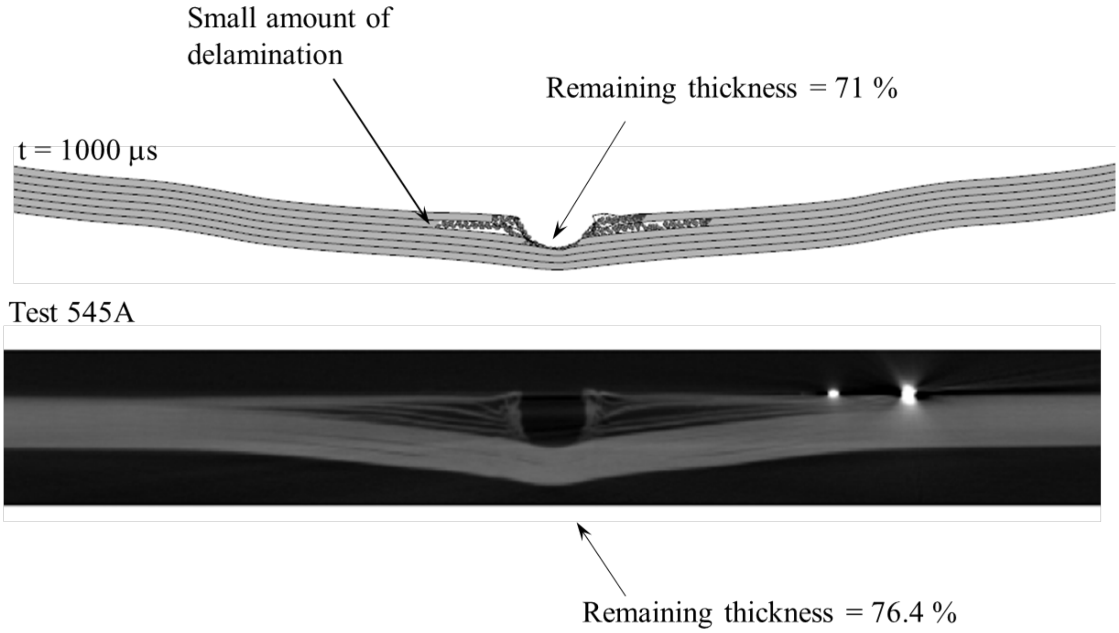
Small amount of delamination
Remaining thickness = 71 %
t = 1000 μs
Test 545A
Remaining thickness = 76.4 %

Figure 22. Comparison of the computed and experimental penetration channel at t = 1000 μs after impact, for an impact velocity of V = 293 m/s.

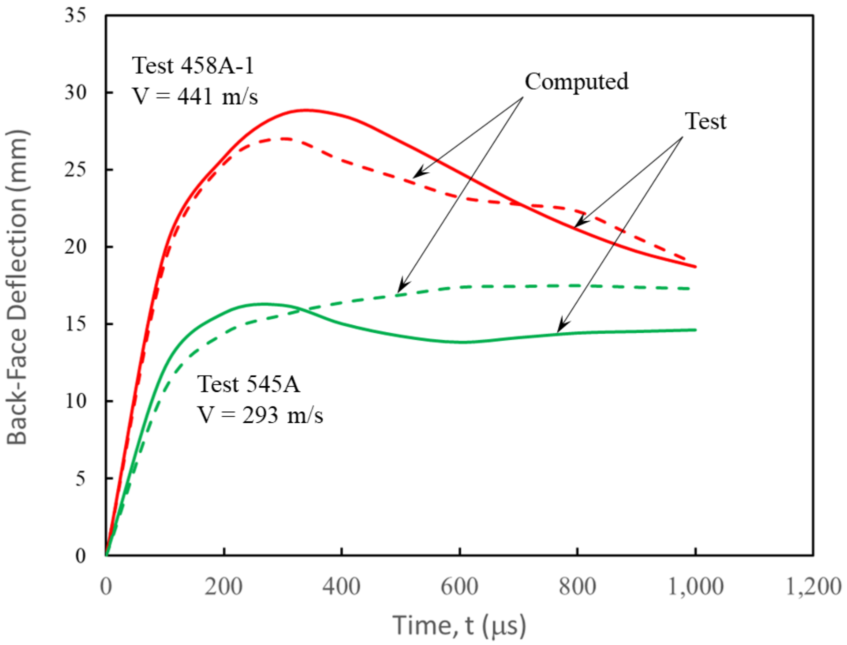

Figure 23. Comparison of the computed and experimental back-face deflections for an impact velocity of V = 293 and 441 m/s.

Three Dyneema® HB80 panel thicknesses were also tested to determine their ballistic limit velocities when impacted by a 0.22-cal FSP as provided by Zhang *et al.* [8]. The panels were 450 mm square with thicknesses of 7.9 mm, 8.9 mm, and 10.9 mm. These panels produced normalized ballistic limits of 1.0, 1.09, and 1.26 respectively (all velocities in this subsection are normalized by the experimental ballistic limit velocity for the 7.9 mm panel). Computations were performed and compared to the experimental results. The material properties used are the same as those used for the BFD computations and the mesh resolution has a minimum of seven layers through the thickness and a uniform mesh throughout.

Figure 24 presents the initial geometry for the 7.9 mm thick panel including the mesh. This configuration uses 7 layers of elements through the thickness (1,845,600 elements total) requiring less than 1 hour to complete on 16 processors. Figure 25 presents the computed results for an impact velocity of V = 1.0 (the experimental ballistic limit) and V = 1.015. The panel stops the FSP at V = 1.0. When the impact velocity is increased to V = 1.015 the panel is perforated. The estimated computed ballistic limit is V_{50} = 1.008 in close agreement with the experimental value of V_{50} = 1.0.

Figure 26 presents the initial geometry for the 8.9 mm thick panel including the mesh. This configuration uses 8 layers of elements through the thickness (4,671,444 elements total) requiring approximately 1.4 hours to complete on 10 processors. Figure 27 presents the computed results for an impact velocity of V = 1.088 (the experimental ballistic limit) and V = 1.079. The panel is perforated at an impact velocity of V = 1.088, but stops the FSP at V = 1.079. The estimated computed ballistic limit is V_{50} = 1.082 in close agreement with the experimental value of V_{50} = 1.088.

Figure 28 presents the initial geometry for the 10.9 mm thick panel including the mesh. This configuration uses 9 layers of elements through the thickness (5,237,512 elements total) requiring approximately 1.7 hours to complete on 10 processors. Figure 29 presents the computed results for an impact velocity of V = 1.168 and 1.155. The panel is perforated at an impact velocity of V = 1.168, but stops the FSP at V = 1.155. The estimated computed ballistic limit is V_{50} = 1.161, 7.8% lower than the experimental value of V_{50} = 1.259.

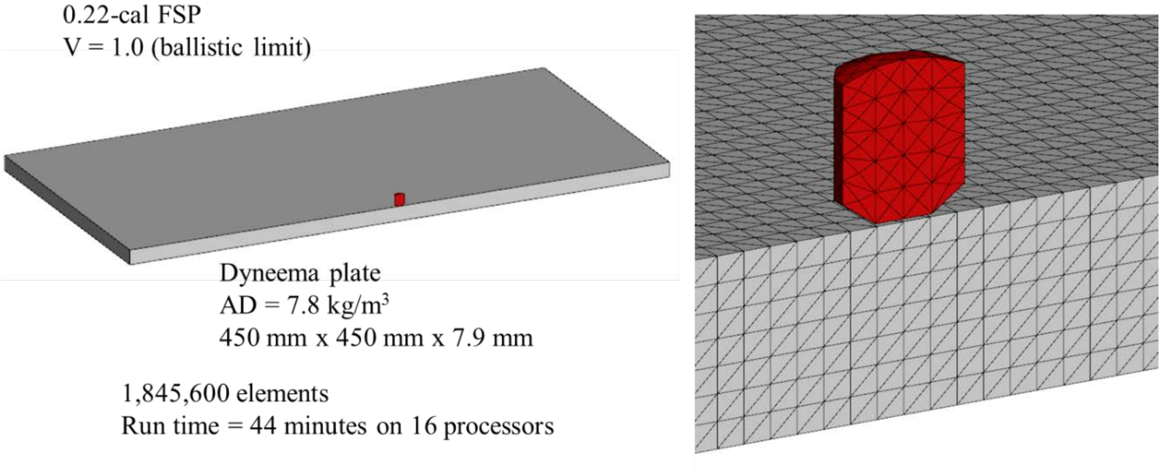

Figure 24. Initial geometry for the 7.9 mm thick panel including the mesh.

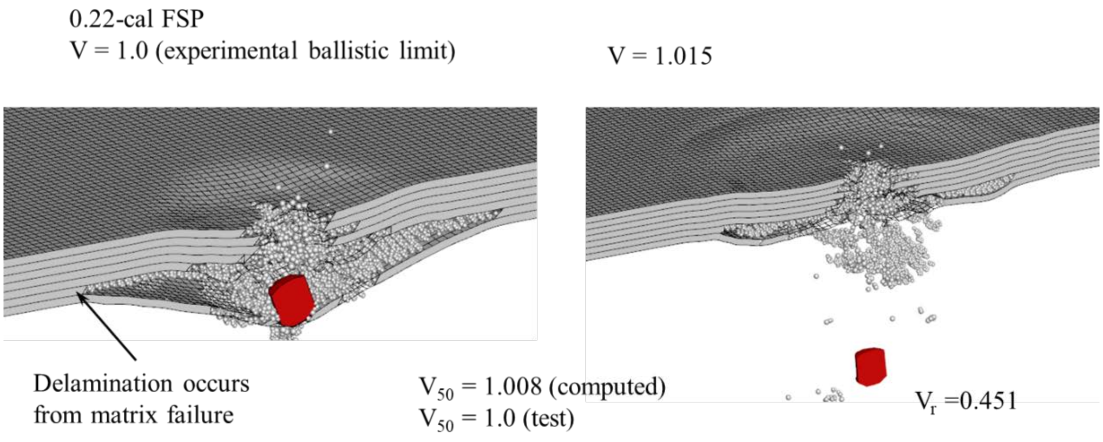
0.22-cal FSP
V = 1.0 (experimental ballistic limit)
V = 1.015
Delamination occurs from matrix failure
V_{50} = 1.008 (computed)
V_{50} = 1.0 (test)
V_r =0.451

Figure 25. Computed results for the 7.9 mm thick panel. The panel stops the FSP at V = 1.0 and perforates the panel at V = 1.015. The computed ballistic limit is estimated to be V = 1.008.

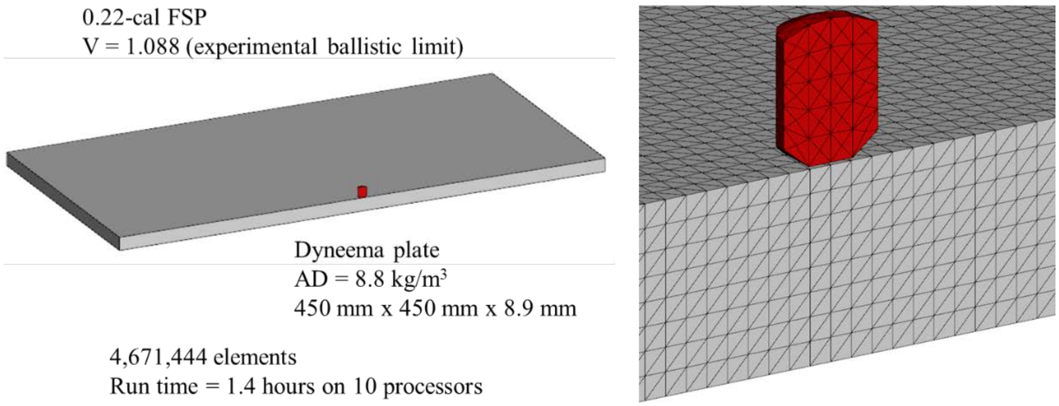
0.22-cal FSP
V = 1.088 (experimental ballistic limit)
Dyneema plate
AD = 8.8 kg/m^3
450 mm x 450 mm x 8.9 mm
4,671,444 elements
Run time = 1.4 hours on 10 processors

Figure 26. Initial geometry for the 8.9 mm thick panel including the mesh.

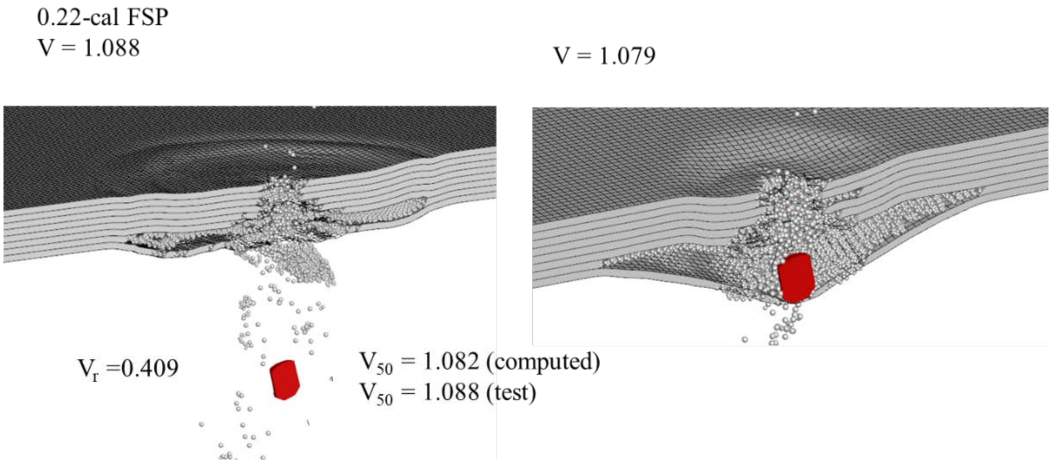
0.22-cal FSP
V = 1.088
V = 1.079
V_r =0.409
V_{50} = 1.082 (computed)
V_{50} = 1.088 (test)

Figure 27. Computed results for the 8.9 mm thick panel. The panel stops the FSP at V = 1.079 and perforates the panel at V = 1.088. The computed ballistic limit is estimated to be V = 1.082.

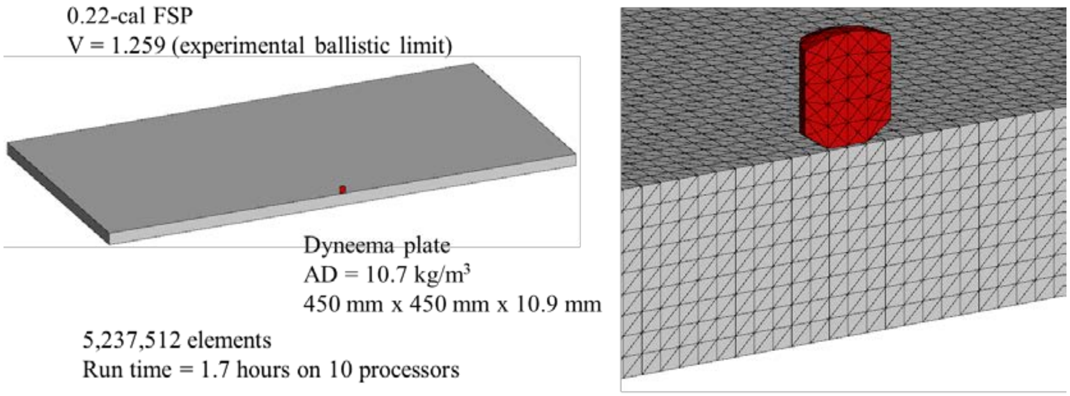
0.22-cal FSP
V = 1.259 (experimental ballistic limit)
Dyneema plate
AD = 10.7 kg/m³
450 mm x 450 mm x 10.9 mm
5,237,512 elements
Run time = 1.7 hours on 10 processors

Figure 28. Initial geometry for the 10.9 mm thick panel including the mesh.

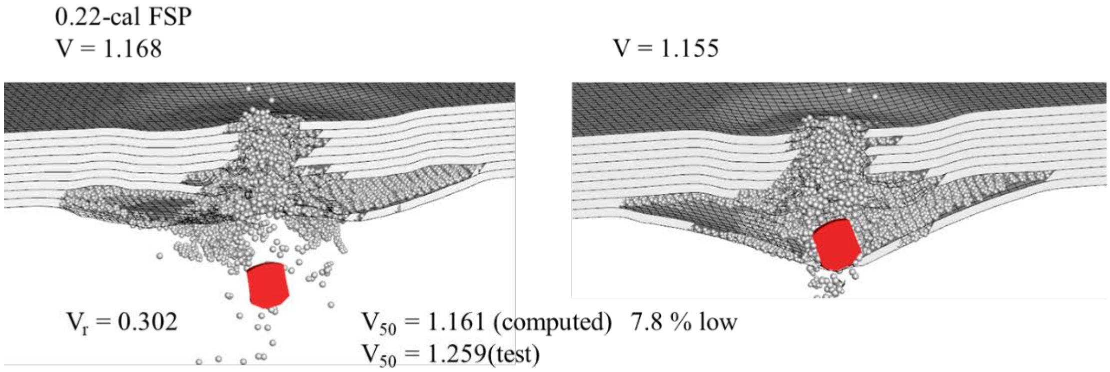
0.22-cal FSP
V = 1.168
V = 1.155
V_r = 0.302
V_50 = 1.161 (computed) 7.8 % low
V_50 = 1.259(test)

Figure 29. Computed results for the 10.9 mm thick panel. The panel stops the FSP at V = 1.155 and perforates the panel at V = 1.168. The computed ballistic limit is estimated to be V = 1.161.

3.4 Elastic Orthotropic Material Model and Cohesive Wedge Elements

This approach uses tetrahedral elements arranged in a symmetric brick configuration (24 tetrahedral elements in a symmetric brick) to describe the response of the fibers and matrix (using an orthotropic elastic material model [13]), and cohesive wedge elements to model the delamination. This is essentially the same approach as presented in subsection 3.2 (using hexahedral elements), but here the hex's are replaced with tetrahedral elements (which are much more robust), arranged in a symmetric brick configuration. The cohesive wedge element is a very new feature, developed with funding from a different program [14]. This new element allows symmetric bricks to be attached providing an approach to model delamination. The cohesive wedge elements use the same cohesive material model developed for hexahedral elements [15].

Figures 30-32 demonstrate this new capability. Figure 30 presents the initial geometry, and mesh, for the BFD configuration presented earlier. Four layers of symmetric brick elements are used to model the fibers and matrix, and three layers of cohesive wedge elements (that attach the symmetric bricks) are used to model delamination. The symmetric bricks use the orthotropic elastic material model with constants provided by Levi-Sasson *et al.* [12], and the cohesive wedge elements use the cohesive material model with estimated constants. Figure 31 presents the computed result for an impact velocity of V = 441 m/s where the sphere is stopped in the target. Figure 32 presents the computed result for an impact velocity of V = 600 m/s where the sphere perforates the target. Both computed results are efficient, robust and demonstrate significant delamination. It should be noted that there are experimental data for the configuration that uses an impact velocity of V = 441 m/s, and the computed result under predicts the maximum back face deflection. It is anticipated that modifications to the material model constants, and a finer mesh, will produce computed results that are in good agreement with the test data.

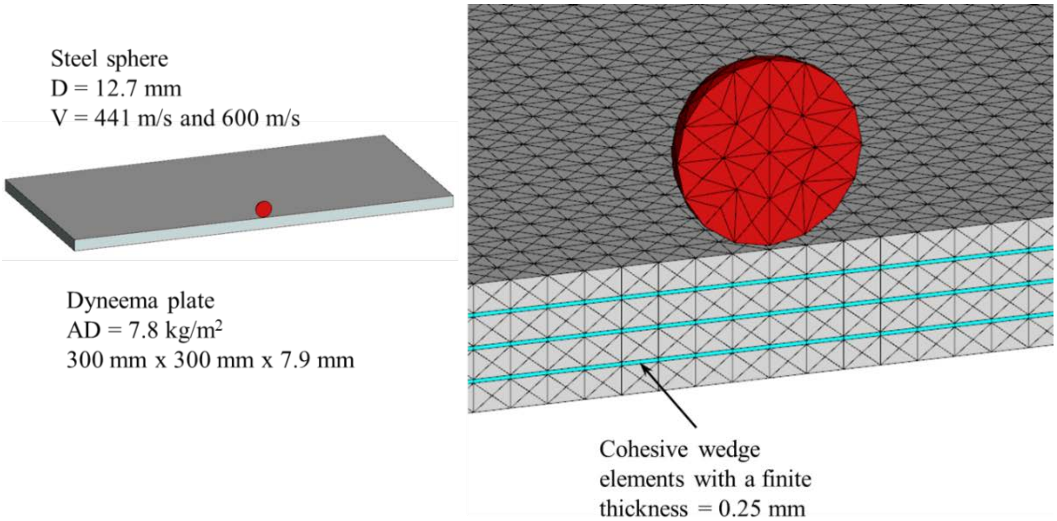
Steel sphere
D = 12.7 mm
V = 441 m/s and 600 m/s
Dyneema plate
AD = 7.8 kg/m²
300 mm x 300 mm x 7.9 mm
Cohesive wedge elements with a finite thickness = 0.25 mm

Figure 30. Initial geometry, and the mesh, for the back-face deformation (BFD) configuration. Four layers of symmetric brick elements are joined together by three layers of cohesive wedge elements.

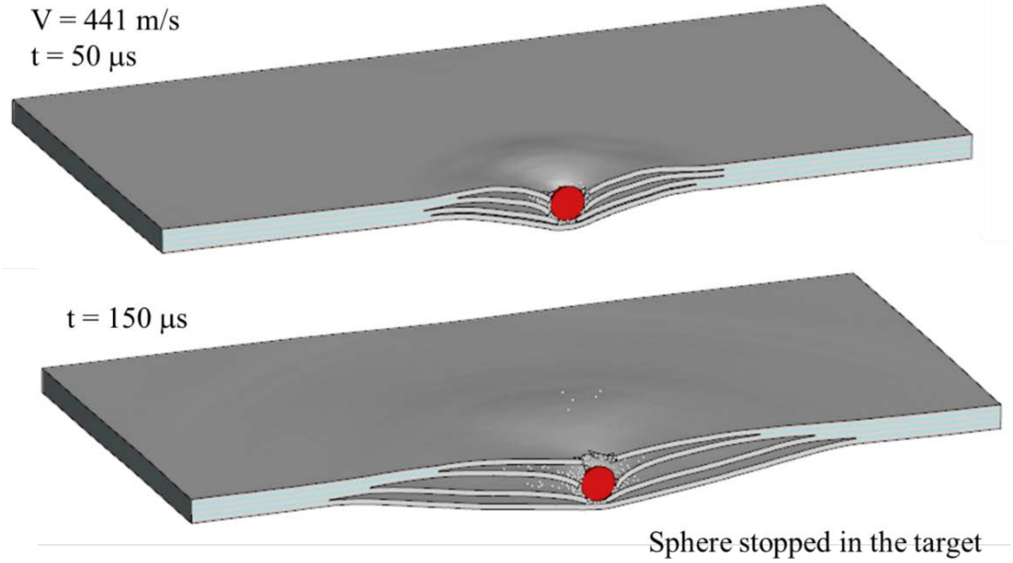
V = 441 m/s
t = 50 μs
t = 150 μs
Sphere stopped in the target

Figure 31. Computed result for a sphere impacting a Dyneema® panel at V = 441 m/s. The sphere is stopped in the target producing significant delamination.

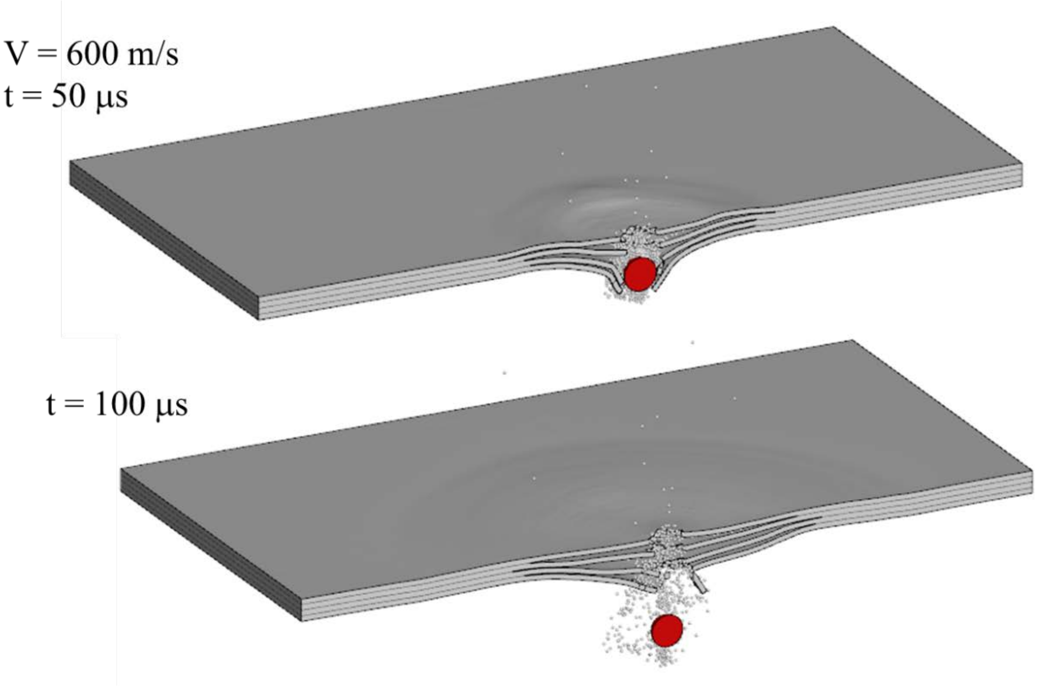
V = 600 m/s
t = 50 μs
t = 100 μs

Figure 32. Computed result for a sphere impacting a Dyneema® panel at V = 600 m/s. The sphere perforates the target producing significant delamination.

4.0 Summary and Conclusions

This report documents two separate computational studies: the first investigated the effect numerical treatment of surfaces and interfaces have on the ballistic response of ceramics; the second evaluated several approaches to model the ballistic response of the composite Dyneema®. The first study investigated target geometries where a ceramic was attached to a metal backing plate and the effect of bonding the plate to the substrate was evaluated. Two target geometries, two projectiles and two ceramics were used including two different ceramic models. Nearly all configurations showed a performance increase when the ceramic was bonded to the back plate (a perfect bond) and there was no configuration that showed a reduction in performance. It is clear from this study that the treatment of interfaces is very important.

The second study evaluated four numerical approaches to model the ballistic response of the composite Dyneema®. The approaches included: hexahedral elements using an elastic orthotropic material model and cohesive elements; a new laminar material model developed at SwRI; 3D bar elements to represent the fibers and solid elements to represent the matrix; and tetrahedral elements (arranged is a symmetric brick configuration) using an elastic orthotropic material model and cohesive wedge elements. Experimental data provided by the ARL were used to evaluate some of the approaches. The use of hexahedral elements was not robust due to severe hourglassing and contact issues and was eliminated as a viable approach. The laminar material model was found to have implementation issues that were addressed under a different contract, but there was not sufficient time to evaluate this approach under this effort; this approach requires further evaluation. The approach that used 3D bar elements and solid elements produced solutions that were in good agreement with all of the experimental data and is the recommended approach although there are some limitations. The approach that used tetrahedral elements using an elastic orthotropic material model and cohesive wedge elements appears to be another good approach although more work on determining the material constants is required.

5.0 References

1. T. J. Holmquist and G. R. Johnson, "Characterization and Evaluation of Silicon Carbide for High-Velocity Impact," *Journal of Applied Physics*, **97**, 093502 (2005).
2. T. J. Moynihan, S. C. Chou, and A. L. Mihalcin, "Application of the Depth-of-Penetration Test Methodology to Characterize Ceramics for Personnel Protection," Army Research laboratory Technical report, ARL-TR-2219, April 2000.
3. A. J. Carpenter, S. Chocron, and C. E. Anderson, Jr., "Bridging the Scales: A Continuum-Based Material Constitutive Model Relating Stresses and Strains at Various Hierarchical Scales in Composites and Fabrics for high-Rate Applications," SwRI Technical Report 18.19018/015, July 2016.
4. T. G. Zhang, S. S. Satapathy, L. R. Vargas-Gonzalez, and S. M. Walsh, "Modeling Ballistic Response of Ultra-High-Molecular-Weight Polyethylene (UHMWPE)," Army Research laboratory Technical report, ARL-TR-7723, July 2016.
5. S. R. Beissel, "Implementation of a Continuum Model for Laminar Composites into the EPIC Code," SwRI Technical Report 18.19018/028, September 2017.
6. G. R. Johnson, S. R. Beissel, and P. M. Cunniff, "A Computational Approach for Composite Materials Subjected to Ballistic Impact," *2nd International Conference on Structural Stability and Dynamics*, December 16-18, 2002, Singapore.
7. B. P. Russell, K. Karthikeyan, V. S. Deshpande and N. A. Fleck, "The High Strain Rate Response of Ultra High Molecular-Weight Polyethylene: From Fiber to Laminate," *International Journal of Impact Engineering*, **60** (2013).
8. T. G. Zhang, S. S. Satapathy, L. R. Vargas-Gonzalez, and S. M. Walsh, "Ballistic Impact Response of Ultra-High-Molecular-Weight Polyethylene (UHMWPE)," *Composite Structures*, **113** (2015).
9. T. J. Holmquist, "Improved Computational Modeling for Advanced Armor – Year 4 (Dyneema Modeling)", SwRI Final Review/Report, July 29, 2014.
10. U. Heisserer., "Tensile Properties of Dyneema HB plies (HB2, HB26, HB50, HB80)," DSM-Dyneema Technical Report, January, 2011 (proprietary).
11. S. Chocron, A. E. Nicholls, A. Brill, A. Malka, T. Namir, D. Havazelet, H. van der Werff, U. Heisserer, and J. D. Walker, "Modeling Unidirectional Composites by Bundling Fibers into Strips with Experimental Determination of Shear and Compression Properties at High Pressures," *Composites Science and Technology*, **101** (2014).
12. A. Levi-Sasson, I. Meshi, S. Mustacchi, I. Amarilio, D. Benes, V. Favorsky, R. Eliasy, J. Aboudi, and R. Haj-Ali, "Experimental Determination of Linear and Nonlinear Mechanical Properties of Laminated Soft Composite Material Systems," *Composites: Part B* **57** (2014).
13. S. R. Beissel, "An Orthotropic Model for Composite Materials in EPIC," SwRI Technical Report 18.19018/006, June 2014.
14. C. Gerlach and T. J. Holmquist, "The Addition of Cohesive Wedge Elements into the EPIC Code," SwRI Technical Report 18.23292, January 2018.
15. S. R. Beissel, "The Addition of a Cohesive Model to the EPIC Code for Simulating Interfaces in Composite Materials," SwRI Technical report 18.19018/017, August 2016.